

AD _____

Grant Number DAMD17-96-1-6192

TITLE: Development of High-Resolution Pet Mammogram Modules

PRINCIPAL INVESTIGATOR: Dr. William Worstell

CONTRACTING ORGANIZATION: Boston University
Boston, Massachusetts 02215

REPORT DATE: August 1997

TYPE OF REPORT: Annual

PREPARED FOR: U.S. Army Medical Research and Materiel Command
Fort Detrick, Maryland 21702-5012

DISTRIBUTION STATEMENT: Approved for public release;
distribution unlimited

The views, opinions and/or findings contained in this report are those of the author(s) and should not be construed as an official Department of the Army position, policy or decision unless so designated by other documentation.

DTIC QUALITY INSPECTED 2

19971210 062

REPORT DOCUMENTATION PAGE

Form Approved
OMB No. 0704-0188

Public reporting burden for this collection of information is estimated to average 1 hour per response, including the time for reviewing instructions, searching existing data sources, gathering and maintaining the data needed, and completing and reviewing the collection of information. Send comments regarding this burden estimate or any other aspect of this collection of information, including suggestions for reducing this burden, to Washington Headquarters Services, Directorate for Information Operations and Reports, 1215 Jefferson Davis Highway, Suite 1204, Arlington, VA 22202-4302, and to the Office of Management and Budget, Paperwork Reduction Project (0704-0188), Washington, DC 20503.

1. AGENCY USE ONLY (Leave blank)		2. REPORT DATE August 1997	3. REPORT TYPE AND DATES COVERED Annual (1 Jul 96 - 30 Jun 97)	
4. TITLE AND SUBTITLE Development of High-Resolution Pet Mammogram Modules			5. FUNDING NUMBERS DAMD17-96-1-6192	
6. AUTHOR(S) Dr. William Worstell				
7. PERFORMING ORGANIZATION NAME(S) AND ADDRESS(ES) Boston University Boston, Massachusetts 02215			8. PERFORMING ORGANIZATION REPORT NUMBER	
9. SPONSORING/MONITORING AGENCY NAME(S) AND ADDRESS(ES) U.S. Army Medical Research and Materiel Command Fort Detrick, Maryland 21702-5012			10. SPONSORING/MONITORING AGENCY REPORT NUMBER	
11. SUPPLEMENTARY NOTES				
12a. DISTRIBUTION / AVAILABILITY STATEMENT Approved for public release; distribution unlimited			12b. DISTRIBUTION CODE	
13. ABSTRACT (Maximum 200) Because of the limitations of standard X-ray mammography for the early detection of breast cancer, in particular for women with radiographically dense breasts, nuclear medicine imaging techniques are of interest for this application. Of these techniques, Positron-Emission Tomography has the greatest potential for high sensitivity to small tumors, and good uptake ratios have been demonstrated for breast tumors with the standard PET radiotracer FDG. The key PET detector attributes for this application are high acceptance and good efficiency at high rates, fine spatial resolution, and good scatter rejection. We are constructing and testing novel prototype PET detector module which have demonstrated high spatial resolution (2.5mm FWHM in all three dimensions when reconstructing a point source), with large acceptance and a unique active-edge and active-corner geometry which will be compatible with standard breast imaging procedures including the imaging of axillary nodes. We plan to continue to optimize and test larger-scale, higher-efficiency, higher-speed and higher-resolution modules within the coming year.				
14. SUBJECT TERMS Breast Cancer Mammography Positron Emission Tomography			15. NUMBER OF PAGES 32	
			16. PRICE CODE	
17. SECURITY CLASSIFICATION OF REPORT Unclassified	18. SECURITY CLASSIFICATION OF THIS PAGE Unclassified	19. SECURITY CLASSIFICATION OF ABSTRACT Unclassified	20. LIMITATION OF ABSTRACT Unlimited	

FOREWORD

Opinions, interpretations, conclusions and recommendations are those of the author and are not necessarily endorsed by the U.S. Army.

____ Where copyrighted material is quoted, permission has been obtained to use such material.

____ Where material from documents designated for limited distribution is quoted, permission has been obtained to use the material.

✓ Citations of commercial organizations and trade names in this report do not constitute an official Department of Army endorsement or approval of the products or services of these organizations.


____ In conducting research using animals, the investigator(s) adhered to the "Guide for the Care and Use of Laboratory Animals," prepared by the Committee on Care and Use of Laboratory Animals of the Institute of Laboratory Resources, National Research Council (NIH Publication No. 86-23, Revised 1985).

✓ For the protection of human subjects, the investigator(s) adhered to policies of applicable Federal Law 45 CFR 46.

____ In conducting research utilizing recombinant DNA technology, the investigator(s) adhered to current guidelines promulgated by the National Institutes of Health.

____ In the conduct of research utilizing recombinant DNA, the investigator(s) adhered to the NIH Guidelines for Research Involving Recombinant DNA Molecules.

____ In the conduct of research involving hazardous organisms, the investigator(s) adhered to the CDC-NIH Guide for Biosafety in Microbiological and Biomedical Laboratories.



PI - Signature

7/29/97
Date

Table of Contents

FRONT COVER:.....	1
Standard Form (SF) 298, REPORT DOCUMENTATION PAGE:.....	2
FOREWORD:.....	3
TABLE OF CONTENTS:.....	4
INTRODUCTION:.....	5
BODY:.....	6
Experimental methods, assumptions, and procedures.....	6
Results and discussion.....	12
Recommendations and future plans.....	15
CONCLUSIONS:.....	16
REFERENCES:.....	17
APPENDICES:.....	18
Development of a High-Resolution PET Detector using LSO and Wavelength-Shifting Fibers.....	18
Characterization of a New Multianode PMT for Low Light-level Optical Fiber Readout.....	23
Monte-Carlo Based Implementation of the ML/EM Algorithm for 3D PET Reconstruction	27

Introduction

There is currently no cure or dependable prevention method for breast cancer, and early detection by breast imaging provides the current best practice for providing effective treatment and reducing mortality. While conventional x-ray mammography reduces breast cancer mortality by about 30% in women over 50 and by 17% in women ages 40-50, x-ray methods have limited sensitivity and specificity for breast cancer detection and diagnosis. Many women have radiodense breast tissue, and in monitoring breast cancer survivors for recurrence scar tissue can make x-ray image analysis very difficult. Overall, roughly 75% of lesions detected by conventional mammography are benign, leading to a large number of unnecessary biopsies; in addition, x-ray techniques give 15-20% false negative results when cancerous lesions are in fact present [1]. These limitations in conventional mammography have given rise to an urgent need to develop novel imaging technologies for more effective early breast cancer detection.

Among potential alternative breast imaging technologies, Positron Emission Tomography (PET) offers a unique combination of demonstrated high sensitivity and high specificity for breast cancer detection, plus the potential for providing new *in vivo* imaging capabilities building on our improving understanding of the molecular biology of breast cancer.[2] PET is a functional imaging modality, and as such is complimentary to the anatomical imaging provided by x-ray, ultrasound, and MRI techniques. In PET, the patient is injected with a short-lived positron-emitting radiotracer which is preferentially taken up by malignant tissues; since positron-emitting isotopes of Carbon, Oxygen, Nitrogen and Fluorine (which serves as a chemical analog of Hydrogen) exist, positron-emitting forms of virtually any biomolecule may be produced, at least in principle. While the great majority of clinical PET studies of breast cancer have been performed with a radioactive form of glucose (FDG = 18F-Fluoro-Deoxy-Glucose) [3-8], a number of pioneering studies have used radioactive taxol, estrogens, and various other ligands [9-11].

PET breast imaging can exploit a panoply of detection instruments as well as a variety of radiotracers; in addition, nuclear medicine provides a number of additional lower-energy planar imaging and SPECT (Single Photon Emission Computed Tomography) modalities and radiotracers under the general appellation "scintimammography".[12] In addition to its great potential for radiotracer diversity, PET is distinguished from scintimammography by higher spatial resolution and lower scatter backgrounds, which should lead to higher sensitivity and specificity for small, early lesions. Within the last few years, several research groups have begun to explore the potential of dedicated PET breast imaging systems, whose greater proximity to the breast should lead to improved counting statistics and higher-quality images. The reduced detector size for a dedicated system typically allows for instrumentation choices which would be quite expensive in large imaging systems, again giving the potential for higher-resolution and higher-quality images. At the time of this writing, we are aware of 5 groups (plus our own) who have proposed or are constructing dedicated PET breast imaging systems, but no clinical results have thus far been presented or published by any group [13-17]. The objective of our ongoing research effort is to construct and characterize components of a dedicated PET breast imaging system which we believe will have technical advantages over its rivals, where these advantages should lead to improved image quality and quantitative accuracy at lesser cost, as well as greater sensitivity and greater accuracy near the physical edge of the detector (for imaging axillae and near the chest wall).

Our two-year research effort is focussed on the design and fabrication of high-resolution PET mammography modules according to our novel design, and on the evaluation and optimization of their anticipated performance as part of a future dedicated PET mammograph. Within the past year we have constructed and tested a succession of prototype modules, and have evaluated their performance in response to sources with known characteristics and geometry. The most important features of our module design and the principal results of key performance assessments will be detailed in the next section, followed by a discussion of our plans for the further assessment of these and successor modules within the coming year.

Body

Experimental Methods, Assumptions and Procedures:

Our detector design is distinguished by its geometry and by its readout method, which combine to give improved high-resolution 3-D imaging capability at reduced cost in comparison to rival techniques. Conventional PET detector module designs use scintillator crystals to serve two purposes: to convert the energy of incident gamma rays to visible light, and to guide this visible light to one or more photosensors which are optically coupled to the crystals. In a conventional detector, one uses an array of small scintillator crystals and various optics/electronics designed to ascertain which crystal converted the gamma ray, with little or no information on where within the crystal such conversion occurred. Typical scintillator crystal geometries are perhaps 3mm x 3mm x 20mm, where the last dimension is dictated by the need for good conversion efficiency for the relatively high-energy 511keV gammas. A pair of such scintillator arrays is needed for PET imaging, since the radiotracer source distribution is tomographically reconstructed from lines-of-response connecting pairs of coincident gamma ray interactions (where these gamma rays have arisen from positron annihilation and the emission of back-to-back gammas).

Since the range of a secondary electron produced in the photocapture reaction of a gamma ray within a dense scintillator crystal is much less than a millimeter, considerable spatial information is lost if the position of interaction within a given scintillator crystal is not measured (as it is not, in conventional detectors). Most importantly, gamma rays which are incident on the scintillator array at oblique angles have significant errors in their coincident lines-of-response, an effect which is usually termed parallax error or depth-of-interaction ambiguity. This effect becomes particularly pronounced in the close-proximity geometry of a dedicated PET breast imaging system, most especially if one seeks to use coincident events with fairly large oblique angles of incidence in order to obtain significant spatial resolution along the axis connecting two opposed detector arrays. Our competitors' dedicated PET breast imaging designs, therefore, either reduce the depth of the scintillator crystals to much less than 20mm and thus have lesser efficiency, or else reject events at large incident angles in what amounts to planar rather than tomographic imaging. The former strategy reduces event statistics and thereby reduces spatial resolution given reasonable limits on the amount of radiotracer injected in the patient, while the latter strategy reduces image signal-to-noise by superimposing overlying tissue on the region of interest.

Our design avoids depth-of-interaction ambiguity by measuring gamma-ray interaction positions before scintillation light has spread far; this is accomplished by configuring our scintillator as a stack of thin, flat sheets (2.5mm x 112mm x 112mm) interspersed with ribbons of wavelength-shifting (fluorescent) optical fibers. These fibers serve as photonic sensors, taking scintillation light as input and providing optically-piped fluorescent light as output. This wavelength-shifted light is then guided to position-sensitive photosensors for readout, thereby measuring the position of the gamma-ray interaction and scintillation light production. Unlike transparent fiber optics, fluorescent fiber optics can accept input light through their sides and pipe it to their ends, so that a "ribbon" of parallel fibers can serve as a incident light position sensor in 1 dimension. We use perpendicular ribbons of wavelength-shifting fibers on opposite sides of our thin scintillator sheets to determine gamma-ray interaction positions in two dimensions, with the third interaction coordinate determined up to the crystal thickness within a stack. For a polished scintillator crystal, only scintillation light travelling nearly normal to flat surfaces may emerge from the crystal without undergoing total internal reflection, due to the high refractive index of the crystal relative to its surroundings. The optical principles underlying our design are further detailed in attached Appendix I: "Development of a High-Resolution PET Detector using LSO and Wavelength-Shifting Fibers", from the Proceedings of the 1995 IEEE Conference on Medical Imaging. The work described in this Appendix directed preceded our USAMARC-funded effort, and culminated in our demonstration of very high spatial resolution for small LSO crystals coupled to wavelength-shifting fibers.

The choice of optimal materials and methods for the construction and readout of high-resolution PET mammography modules with wavelength-shifting fiber readout has been a major part of this year's effort, and the basis for our design choices will be discussed in the "Results" section which follows. We have extensively tested the available design options at each step in the optical and readout chain. This testing has been carried out with a nearly point-like positron source (Na-22) which was collimated for testing module components and single modules, and then used for coincidence testing of pairs of prototype modules. The critical performance parameters measured included system spatial resolution, energy resolution, timing resolution, efficiency, light yield (which correlates with the robustness and efficiency of the fiber coordinate measurement), and rate capability. We have used a 50 microcurie source for most tests, where this is approximately the total activity expected within a breast during a PET mammograph scan.

One of the most important design choices comes at the beginning of the optical chain, with the choice of scintillator. In our proposal we planned to use LSO or Lutetium Oxyorthosilicate, and we have been able to obtain 100cc's of this material for the construction of test modules. Unfortunately, this proprietary material has until very recently (just this month) been unavailable outside of CTI/Siemens's internal development program, so that we have switched to a less expensive and more readily available scintillator for our initial work. We selected CsI(Na), Sodium-doped Cesium Iodide, based upon its high light yield, ease of working, and relatively low cost; as will be discussed below this choice has placed some limits on our achievable spatial resolution and timing/rate capability, but it has allowed us to construct many prototypes rapidly with which to explore design issues which are common to CsI(Na) or LSO-based devices. Given the order-of-magnitude lower cost of CsI(Na) relative to LSO, there is significant motivation for obtaining good performance with a CsI(Na) device; we have succeeded in obtaining funding for limited clinical application of a larger-scale successor CsI(Na) imaging system from the Commonwealth of Massachusetts's Breast Cancer Research Program under the title "Cost-Effective High-Resolution Positron Emission Mammography." We nonetheless intend to continue development of modules using LSO scintillator as well as CsI(Na)-based modules, and we have 100cc's of LSO currently in hand which we are preparing for incorporation into two single-layer modules each 112mm x 112mm x 2mm thickness. Tests on these LSO modules will be carried out in the coming year, and we will acquire sufficient LSO for two 3-layer LSO modules, as planned.

Our most important design assumption to date has been that the radiation environment (source strength and distribution, background rates, etc.) in which we are testing our prototypes is comparable to that which will be experienced in an actual mammography module during a clinical PET imaging procedure. Our source activity estimates are based upon measurements which were performed with conventional whole-body PET scanners and reported in the literature, combined with estimates of activity outside the field-of-view (such as the radiotracer uptake in the heart, particularly for FDG) and its expected contribution to backgrounds by scattering into our detectors. These are rough estimates and we have yet to carry out careful analyses of optimal screening of activity outside the field-of-view, since we expect the most useful input information for such an analysis to come from experience with our actual modules in future clinical application. Such future measurements, and any forms of human use, are beyond the scope of our research program as funded by the USAMARC and detailed in our statement of work, but planning for them has had a significant impact on our detector design. For example, we have constructed our prototypes to have an "active edge" and an "active corner" based on discussions with clinicians who emphasized the importance of axillary nodal imaging and of imaging tissues near the chest wall. We have made every effort to make our device geometry compatible with breast imaging practice as carried out in x-ray mammography (although we anticipate much less compression to accompany our considerably longer scans), and we have gone so far as to obtain a donated mammography stand which we are outfitting with mechanical fixtures to mount our prototype detectors and their clinical successors. Our intention is to move our research from the laboratory to the clinic at the earliest reasonable date, and our eyes are steady on this future transition.

Detector Design and Construction:

As mentioned earlier, the details of our prototype detector design have evolved through several iterations of a construction/test cycle, and have been informed by a variety of component-level tests and computer simulations. The experimental findings upon which we have based our most significant design decisions are detailed below:

1) Crystal geometry and surface preparation:

Our crystal geometry of 112mm x 112mm x 2.5mm was based upon readout through 8 ribbons each on the x- and y- surfaces of each crystal, where each ribbon is 14mm across. This 14mm number arose from measurements on early production units of the Hamamatsu R5900-L16 position-sensitive photomultipliers which we use to read out the fibers; more recent units have shown good performance for 16mm width ribbons, so that future crystal dimensions of 128mm x 128mm x 2.5mm are appropriate. The 2.5mm thickness was based upon a target resolution of 2.0mm FWHM, which we expect to be a good match to the statistical limits in image quality available for a high-efficiency PET mammography unit for anticipated clinical doses and scan times. The actual resolution obtained with CsI(Na) is 2.5mm, due to Compton scatter interactions within the large, flat scintillator crystals as discussed further below. Rather than decrease the crystal thickness further, which would increase the number of layers required for an efficient detector, we expect to keep the same thickness until we have more experience with clinical experience with successor prototypes. For LSO-based modules, we would anticipate a crystal thickness of 2.0mm in order to take advantage of the higher density, faster timing, and higher photofraction of this material relative to CsI(Na); in both cases, a full-thickness module is expected to incorporate 7 layers of crystal read out through 8 fiber ribbons.

The quality of the scintillator crystal surface finish is important in our application for two reasons: first, because we require a clear division between light which is totally internally reflected within the crystal and that light which emerges from the crystal into the fiber ribbons, and second because we need the overall crystal/fiber laminated stack to be transparent to wavelength-shifted light. We require such transparency because in our device we have separated the functions of interaction position measurement (through the fiber readout) from gamma ray energy measurement and triggering/timing (through an Anger array of photomultipliers which view each stack). Because both the scintillator crystals and the fibers are transparent to the wavelength-shifted light, photons traversing the wide range of optical indices within the stack (fiber core, fiber claddings, optical coupling agent, scintillator coating, and scintillator crystal) are scattered rather than absorbed; small scratches on the crystal surface from imperfect polishing, however, absorb light and can cause excessive attenuation of wavelength-shifted light within the laminate. In our devices, we surround the laminated stack by reflective material on all sides except that side with the Anger array, and we are able to obtain good energy and timing resolution as well as good uniformity of response. Because CsI(Na) does not readily polish to an optical finish and because it is somewhat hygroscopic, considerable effort was needed in order to obtain an adequate surface finish (using silicon oil and progressively smaller sizes of Aluminum Oxide powder abrasives). Our final procedure yielded less than 10-20% variation in light collection from one side of the stack versus the other, which is readily corrected since the depth of interaction in the stack is measured.

The effect of imperfect surface preparation for CsI(Na) was more difficult to analyze, and determination of the role of scintillation light scattering from crystal surface imperfections (rather than totally internally reflecting) required a great deal of experimentation. These experiments were complicated by the fact that the radioactive source we were using to assess our system's spatial resolution turned out to have considerable extension; although specified to have active dimensions of 1mm x 1mm x 1mm at the time of its purchase, it turned out to be a disk roughly 5mm in diameter and perhaps 1mm in thickness. Once we realized that we had been imaging our sources's extension rather than measuring our device's resolution, we had built special test modules with

1mm-deep reflector-filled grooves at 2mm intervals across each crystal surface -- in order to limit light spreading away from the interaction region within each scintillator crystal. When imaging the smallest dimension of our disk-shaped source, we then found no difference in spatial resolution between the grooved modules and earlier ungrooved modules, eliminating the hypothesis that our observed 2.5mm limiting resolution was due to light spreading. This limiting resolution was also insensitive to the amount of light collected by the fibers, which was a tip-off that it was either due to source extension or to non-pointlike light production in the scintillator crystal.

Finally, we were able to determine that our imaging resolution for 2.5mm thick plates of CsI(Na) is limited by Compton scattering and secondary photon capture within a single plate. The true photofraction (ratio of photocapture events to all gamma-ray interactions) for 511 keV gamma rays in CsI(Na) is about 15%, while the apparent photofraction (fraction of events within the photopeak for 511 keV gammas normally incident on a 2.5mm thick plate) is more than 25%. The difference arises from gammas which Compton scatter at 90 degrees, followed by photocapture of the secondary gamma rays. These secondary gammas have energies near 250 keV and a range of about 7 mm in CsI(Na); computer simulations show a limiting resolution due to this effect close to our observed 2.5mm FWHM, for two detectors in coincidence. For a CsI(Na) device, this effect can be somewhat lessened with thinner crystals, which increases the fraction of "true" photocaptures within "apparent" photocaptures (by decreasing the angular acceptance for secondaries to convert in the same crystal) but this either increases the number of detector layers required or decreases the overall efficiency. For LSO devices the effect is much less pronounced because of the higher true photofraction for LSO (30%) and the factor of 2 shorter attenuation length for the secondary gammas in this denser material relative to CsI(Na). In fact, it was because our earlier tests on fiber readout of LSO had shown such good spatial resolution that we were somewhat surprised by the magnitude of this effect in CsI(Na).

2) Optical coupling of crystals to fibers:

Our second round of prototype modules (the first had attenuation difficulties due to imperfect crystal surface treatment) yielded a significantly lower fiber light yield relative to the first, for reasons which were not understood at first. After some experimentation, we discovered that the effect was due to a relatively high-index optical epoxy which we used to coat the hygroscopic crystals; once we determined that the crystals did not degrade with ambient humidity over a time scale of 1-2 weeks (the time between cutting/polishing and sealing them into laminated modules) we omitted the coating step. Although the crystals did not degrade, the greater optical index mismatch without the coating trapped more light within the crystal and decreased our fiber light yield. In the third round of prototypes, the light yield was restored and slightly improved by introducing a crystal coating layer with refractive index near the geometric mean between that of the crystal and that of the fiber outer cladding; this thin layer then serves as an antireflection coating. There is still sufficient light trapped within each crystal to be collected at the perimeter of each crystal within a stack, however, as will be described in the module assembly section below.

3) Fiber selection and preparation:

We experimented with both round and square cross-section fibers, with different fluor formulations and concentrations, and with diameters ranging from 0.5mm to 1.0mm. Round fibers gave nearly a factor of two better light yield relative to square fibers, which we traced to much smaller attenuation losses along the fibers with round cross-sections. This arises because the square fibers do not have a precisely square cross-section, leading to optical ray paths which encounter the core/cladding interface at more than the critical glancing incidence angle. This effect may be evidenced by shining a flashlight on the side of a fiber ribbon in a darkened room -- this flashlight test also proved useful when examining detector modules for any fiber damage such as nicked cladding. Similarly, 1mm fibers had significantly higher light yield than 0.5mm fibers, in this case due to self-absorption to the limited Stokes shift between absorption and emission,

combined with the higher fluor concentrations required for efficient fluorescent in 0.5mm fibers. Finally, BBQ-doped fibers did not yield a significantly higher light yield than our standard BCF-91A formulation when coupled to CsI(Na) crystals. We have used multi-clad fibers in all prototypes (which earlier tests showed superior to single-clad fibers) and succeeded in obtaining 50% light yield improvements by optically coupling aluminized mylar mirrors to the ends of polished fiber ribbons. This last was used to obtain two active edges and an active corner away from the readout ends of the fibers.

4) Multilayer stack assembly and fixing:

Multilayer crystal/fiber stacks were built up from acrylic "frames" 3.5mm thick, with cutaway regions on one side to guide a 1mm thickness fiber ribbon, and a square opening in the center to position the 112mm x 112mm coated crystal. Fiber ribbons were first glued to frames, then a stack was built up by placing coated crystals onto fibers within each frame, with the axes of the fiber ribbons alternating between two orientations as the stack was built up. We then fixed the assembled stacks by casting them in an epoxy resin (Emerson & Cummings potting compound Stycast 1367). We devoted considerable effort to developing procedures which allowed the potting compound to fill all interstices without generating air gaps or bubbles, and we succeeded in casting nearly defect-free 7-layer stacks. For each stack, the top layer contained fibers only, so that a stack with 7 crystal layers has 8 fiber layers; this is required in order to obtain x- and y-coordinate information from all crystals in the stack. Wavelength-shifting fibers were also coupled to the perimeter of each crystal in a stack, with these fibers read out separately to determine the depth-of-interaction within a stack (these fibers detected the light which was trapped in a crystal layer and guided to the perimeter through total internal reflection). We obtained a light yield of about 10 photoelectrons for 0.5mm diameter perimeter fibers, which is more than sufficient to determine depth-of-interaction to within the crystal thickness of 2.5mm. The top of each module was epoxied to a 5cm-thick "light mixer" which was later coupled to four 2" diameter photomultipliers in an Anger array. The bottom of each module was optically coupled to reflecting material after assembly, as were the edges of the light mixer and those regions of the light mixer not covered by Anger PMTs. Fiber ends which were not read out were polished and optically coupled to aluminized mylar mirrors.

5) Fiber ribbon routing, multiplexing, and readout coupling:

To date we have been reading out only single-layer modules (i.e. a single crystal layer coupled to 8 x 14mm width x-ribbons and 8 x 14mm width y-ribbons). Initial testing was performed with no readout multiplexing, reading out just 4 x-ribbons and 4 y-ribbons through 8 multianode photomultipliers. This was followed by multiplexed readout of two ribbons per multianode photomultiplier, where a rough coordinate from the Anger PMT array was used to demultiplex between the two ribbons on each fiber readout PMT. For our initial Anger optics it was two ribbons 4 x 14mm apart were very easily distinguished, as were two ribbons 2 x 14mm apart near the center of the module. However, the edgemost ribbon and that 2 x 14mm further toward the module center had a small amount of overlap; further improvements in the Anger optics would thus be required for four-fold lateral multiplexing (i.e. reading out 8 ribbons with 2 position-sensitive photomultipliers). There is sufficient photocathode area on our multianode photomultipliers to permit both 4-fold lateral multiplexing and 4-fold multiplexing in depth when using 1mm diameter fibers, but now it appears such heavy multiplexing will not be needed because of the new multianode photomultiplier options discussed in the next section. Given the \$1000 price of each multianode photomultiplier it is important to keep their numbers down, but heavy multiplexing decreases system rate capability by introducing pile-up and demultiplexing errors at high event rates. This is much more the case for CsI(Na), with its 700ns decay time, than for LSO with its 70ns decay time, but with the new multianode photomultipliers we can greatly reduce the optical multiplexing while keeping PMT counts down.

In all cases, fibers were optically coupled to multianode PMTs by inserting fiber ribbons into custom-built vises, polishing the fiber ends, then optically and mechanically coupling to the multianode PMTs by attaching the vises to custom PMT mounting mechanics. We found that coupling fibers to PMT photocathodes with silicon optical coupling compound was sufficient to reproducibly produce a uniform and high-efficiency coupling; this method was conducive to the testing of alternative fiber multiplexing schemes by easily making and breaking optical contacts.

6) Multianode photomultipliers and associated electronics:

We used Hamamatsu R5900-L16 multianode photomultipliers to read out the fibers, where each multianode PMT contained 16 separate photocathode regions each 16mm x 1mm. The 16 anodes were resistively coupled in a chain and read out through charge division; details of this readout and measurements of the PMT response are given in Appendix II: "Characterization of a new Multianode PMT for Low Light-level Optical Fiber Readout", from the Proceedings of the 1996 IEEE Nuclear Science Symposium and Medical Imaging Conference. We were able to obtain spatial resolution of less than 1mm FWHM for 8 photoelectrons incident through a single 1mm fiber; our spatial resolution is therefore not limited by our PMT readout, but rather by upstream optics. The two charge-division outputs (whose ratio give the transverse coordinate for light incident through a fiber ribbon, and whose sum gives the total fiber light yield) were read out through custom-built 4-PMT bases and coupled to x10 charge-sensitive preamplifiers which we also constructed. The single photoelectron peak from the multianode photomultipliers was very pronounced, simplifying detector gain calibration considerably. Spatial calibration of the detector was also straightforward when imaging a point source, and 3-4mm FWHM resolution was obtainable with no calibration constants at all. Boundary effects between adjacent fiber ribbons were found to be minimal, and determination of interaction coordinates was robust and unambiguous because of the substantial fiber light yield (averaging 8 photoelectrons/511 keV interaction) and because of the intrinsic linearity of interaction position measurement through local light collection by fibers. The coordinates obtained were also accurate to the very edge of each prototype detector, as opposed to the Anger coordinates which were quite distorted near each edge.

Although our tests to date have been carried out with R5900-L16 photomultipliers, we have also purchased several R5900-M16 photomultipliers with 16 anodes each 4mm x 4mm arranged in a 4 x 4 array. These will be used to read out depth-of-interaction fibers, and were intended to test readout with less multiplexing at the cost of lesser spatial resolution at the PMT. Very recently, additional options have become available from Hamamatsu Photonics within the R5900 series of devices; in particular, they have produced the R5900-M64 photomultiplier with 64 anodes each 2mm x 2mm arranged in an 8 x 8 array. This device will be capable of 8-fold parallel charge-division readout of 16 1mm-thickness ribbons each with just 2-fold multiplexing; another interesting option is to interdigitate fibers within a 32mm diameter x 1mm thickness ribbon to make a 16mm x 2mm block, where the spatial resolution will still be dominated by the upstream optics, at least for CsI(Na) devices. The high speed of LSO permits greater multiplexing without penalty.

7) Data acquisition electronics and computer interface:

We used commercial LeCroy 2249W ADCs to digitize the outputs of both 4 Anger PMTs per module and 16 multianode PMT charge-division outputs per module. A trigger was generated from the coincidence of discriminated output of analog-summed Anger PMT signals, and each of the 40 digitized signals was delayed by 200ns to land within a 1000ns-width gate. A second, lower threshold was also set on each Anger PMT sum, and the outputs of these discriminators sent to a LeCroy 2228 TDC to determine the coincidence time resolution as a function of threshold. CAMAC readout of the 42 detector channels was performed with a crate controller design at the Budker Institute for Nuclear Physics in Siberia, which is capable of nearly 10KHz readout of this many channels and is coupled to a PC. This rate exceeds that obtainable with commercial CAMAC interfaces by more than an order of magnitude.

Results and Discussion:

We have measured the response of our prototype mammograph modules and obtained the following performance levels to date:

1) Spatial resolution:

We have obtained better than 2.5mm FWHM (Full Width at Half Maximum) spatial resolution in imaging a point-like source; most recently, a point spread function of less 2.0mm FWHM, measured from a "point source" which in fact had some extension, was obtained experimentally and is illustrated in Figure 1 on the following page.

2) Light yield:

We have obtained an average of 8 photoelectrons at the fiber readout for 1mm fibers, 10 photoelectrons for 0.5mm fibers coupled to the periphery of 112mm x 112mm x 2.5mm CsI(Na) crystals, and roughly 200 photoelectrons at the Anger PMT readout. The inordinately small Anger PMT light yield is due to a combination of several effects: incomplete photocathode coverage by 4 2" round PMTs (we have purchased and obtained 60mm square PMTs for successor modules), relatively low PMT quantum efficiency for the green wavelength-shifted light, and less than optimal reflectors about the module edges (we plan to substitute white Tivek reflectors for the aluminized mylar in future modules, and to get better geometric coverage). We anticipate increasing the overall Anger light yield to roughly 400 photoelectrons/511 keV photocapture.

3) Energy resolution:

We have obtained 20% energy resolution FWHM, after correction for nonuniformity in the Anger PMT light collection across the module (this calibration is straightforward, given the fiber-derived event coordinates and the 511keV photopeak). Of this, about 14% FWHM is intrinsic nonuniformity, and about 14% due to our limited photostatistics (these effects add in quadrature). Therefore, we anticipate a future energy resolution of about 15% FWHM for CsI(Na) modules. This should be adequate for clinical scatter rejection requirements, but further tests are needed.

4) Timing resolution:

We have obtained 50ns FWHM timing resolution for CsI(Na) modules by using a second low threshold on the Anger sums in addition to the threshold used for energy/trigger discrimination. This is in agreement with the decay time of the CsI(Na) and the results from computer simulation of the best timing achievable as a function of integration time and threshold level. Given the order of magnitude fast decay time of LSO, we would expect an achievable LSO time resolution of 5ns or better. Time resolution is important for randoms rejection, particularly at high event rates with efficient detector modules.

5) Rate capability:

Our tests to date have been with inefficient single-layer modules, which have obtained singles rates of about 100Khz and trues rates of about 1Khz when in close proximity to our 50 microcurie test source (10cm separation between detector modules). The signal-to-noise ratio should stay about the same while our even rate increases as we move on to higher-efficiency multilayer detector modules. For two 7-layer modules we expect a nearly 50-fold increase in event rates, which will saturate our current data acquisition (DAQ) system with 50 microcuries in the field of view. For this reason, we are currently working to upgrade our DAQ to incorporate custom ADC modules with a PCI interface, designed to be capable of up to 100 KHZ event rates.

Figure 1 (left): Point Spread Function

Cross-section in x of the reconstruction of data from a disk-shaped source of positrons, with source dimensions about 6mm diameter by 1mm thickness -- the thin axis of the disk was oriented along the x-axis. Units are in millimeters, and the FWHM (full width at half maximum) is less than 2mm. Backgrounds due to randoms have been subtracted.

Figure 2: (right) Image of Point (disk) Source

The source was oriented as in Figure 1 (see above). The horizontal coordinate is x, the vertical coordinate is y, all units are in millimeters, and 10 contours of equal intensity are shown.

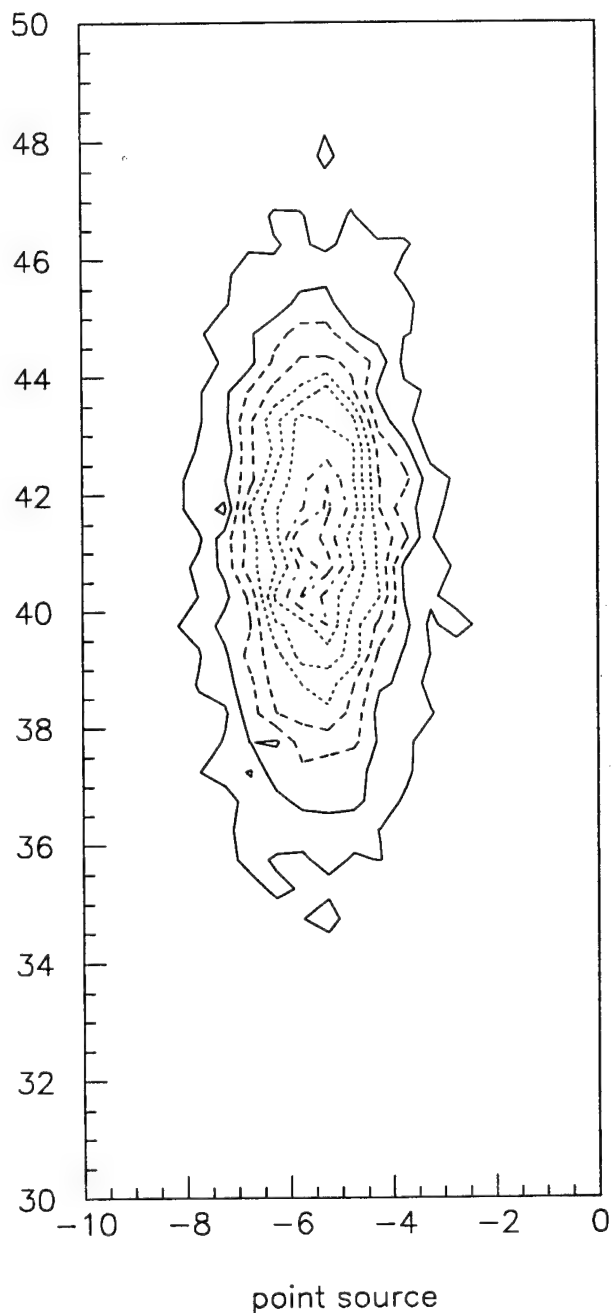
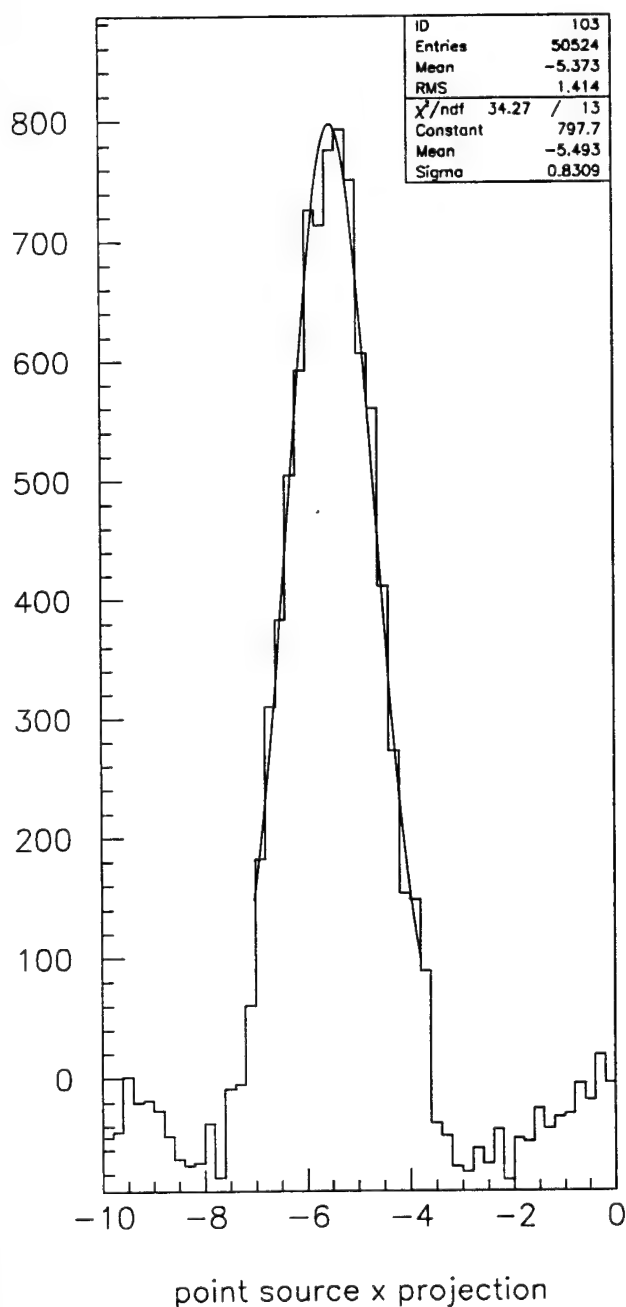
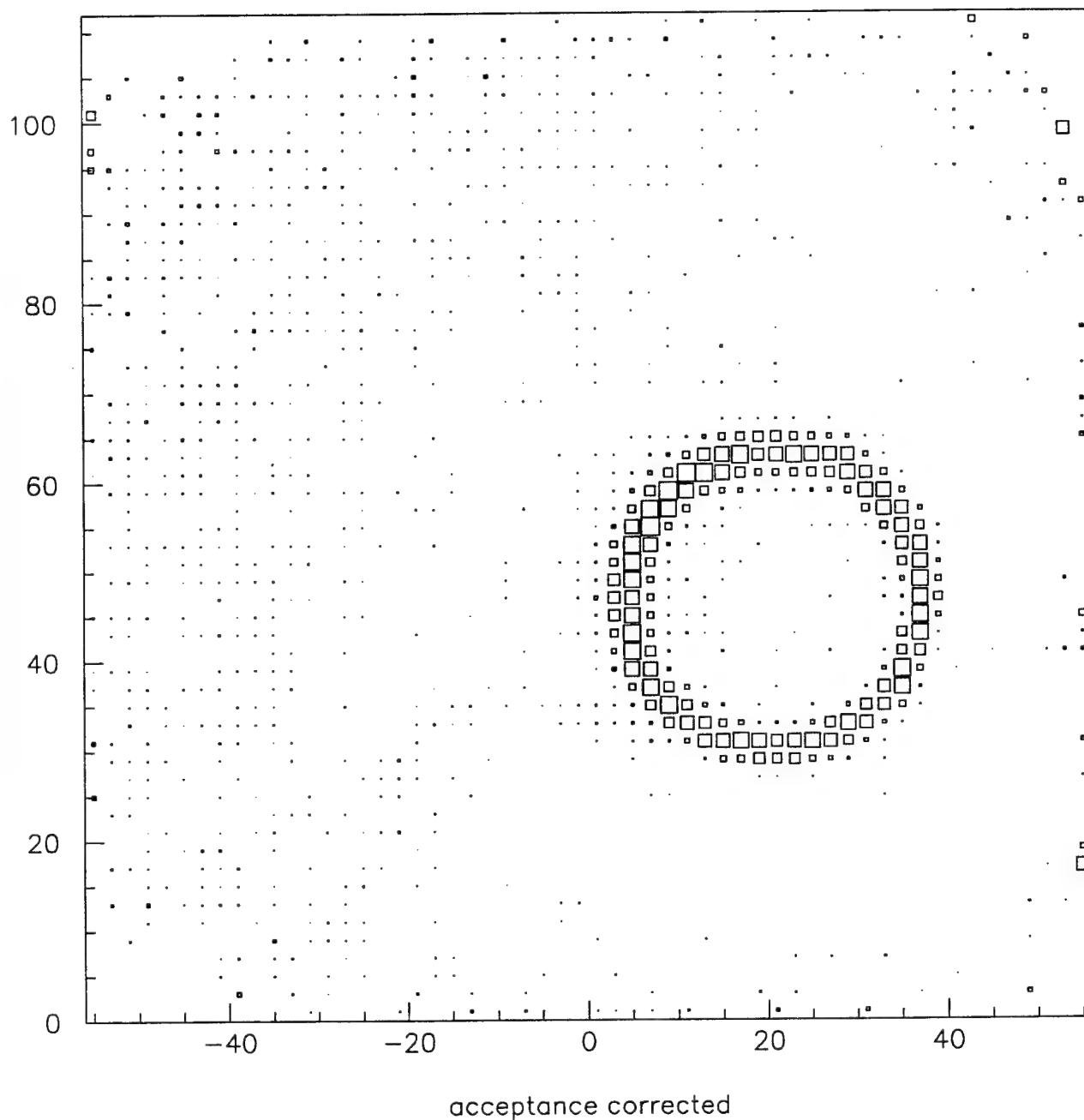


Figure 3: Image of Ring Source

In this image, the disk source described in Figure 1 and Figure 2 was rotated on a spinning wheel, with the disk thin axis (1mm thickness) pointing radially from the center of the circle. All units are in millimeters, randoms have been subtracted, and we have corrected for detector acceptance while accepting all oblique collection angles which struck both detectors. The resulting intensity is uniform over the ring, and statistical errors in background subtraction are amplified by the acceptance correction to large values only very near the edges of the field of view.



Recommendations and Future Plans:

We expect to build upon our current design to construct prototype detectors with greater efficiency, higher rate capability, and improved spatial resolution. Higher efficiency will first be obtained by implementing multi-layer CsI(Na) modules, starting with 3 crystals/4 ribbons, and progressing to 7 crystals/8 ribbons. Higher rate capability will first be obtained by substituting FERAs (Fast Encoding and Readout ADCs) for our current LeCroy 2249 ADCs, while still keeping a CAMAC interface for data acquisition. Later in the year, we expect to fully convert to custom ADCs and a PCI interface which are currently under development. Improved spatial resolution should be obtained with LSO modules, which will start as single-layer modules (the crystals for which are currently being cut and polished) and then will progress to 3-layer modules before the end of the coming year.

Testing of our modules should make the transition from our Na-22 "point" source (which as noted earlier is a 6mm diameter disk with 1mm thickness) to a variety of phantoms which we will fill with F-18 or various liquids; we have made arrangements to obtain and transport this material from the cyclotron at the Massachusetts General Hospital, and we are currently awaiting radiation safety committee approval to commence phantom filling and transportation. The first planned "phantom" is hypodermic needles with 1mm inner diameter, which will provide line source of precisely known geometry. The next phantom will be a custom-designed object with a "DeRenzo" pattern (6 different diameters of hot-spots in 6 sectors of a circle, arrayed on the vertices of equilateral triangles at separations of 3 times their diameter--ranging from 1mm diameters at 3mm separations to 3mm diameters at 9mm separations) with a total thickness of less than 5mm. This will be our "2d" phantom, and it is currently in production at our machine shop. Finally, we plan tests with our "3d" phantom which is a commercial "Micro Deluxe" phantom we have purchased from Data Spectrum corporation, with a similar pattern but as cold rods rather than hot spots, and with a 70mm length along its symmetry axis. Although this "3d" phantom is in fact symmetric along one axis and thus is the same at different z-slices, we will be doing 3-d imaging and reconstruction when we accept events at oblique incidence and seek to accurately reconstruct its entire enclosed volume.

Reconstruction, including background subtraction and perhaps attenuation and scatter correction, will be carried out with a novel iterative reconstruction algorithm which we have developed and which is described in Appendix III: "Monte-Carlo Based Implementation of the ML/EM Algorithm for 3D PET Reconstruction". Iterative reconstruction permits 3d limited-angle tomography, such as is our case with two modules which do not entirely surround the region of interest (e.g. a breast or axillary tails). Accurate reconstruction of the phantoms mentioned earlier are a necessary prerequisite to later clinical application of these or successor modules (where such clinical applications again are beyond the scope of this project as funded by USAMARC).

Finally, we are working to cut the "umbilical cord" of electronics and mechanical mounts which currently restrict our test modules to our laboratory, and to construct new modules connected to portable electronics and a portable data acquisition system, mounting on our donated mammography stand. Our intention is to transport our prototype modules to a clinical setting at the earliest possible date, and if possible we will perform some simple measurements in a clinical setting to ascertain the radiation environment which these modules will encounter in clinical practice. We anticipate simulating such environment by positioning distributed activity throughout the regions outside the field of view during phantom studies toward the end of next year, as we approach the end of this program.

Conclusions

Because of the limitations of standard X-ray mammography for the early detection of breast cancer, in particular for women with radiographically dense breasts, nuclear medicine imaging techniques are of interest for this application. Of these techniques, Positron-Emission Tomography has the greatest potential for high sensitivity to small tumors, and good uptake ratios have been demonstrated for breast tumors with the standard PET radiotracer FDG. The key PET detector attributes for this application are high acceptance and good efficiency at high rates, fine spatial resolution, and good scatter rejection. We are constructing and testing novel prototype PET detector module which have demonstrated high spatial resolution (2.5mm FWHM in all three dimensions when reconstructing a point source), with large acceptance and a unique active-edge and active-corner geometry which will be compatible with standard breast imaging procedures including the imaging of axillary nodes. We plan to continue to optimize and test larger-scale, higher-efficiency, higher-speed and higher-resolution modules within the coming year.

References

- [1] Kopans OB. "The positive predictive value of mammography." *Amer. J. Rad.* 158:521-526 (1992).
- [2] Jones T. "The Role of Positron Emission Tomography within the Spectrum of Medical Imaging" *Euro. J. Nucl. Med* 23: 207-211 (1996).
- [3] Wahl RL, Cody RL, Hutchings GD, Mudgett EE. "Primary and Metastatic Breast Carcinoma Initial Clinical Evaluation with PET and Radiolabeled Glucose Analog 2-[F-18]-fluoro-2-deoxy-D-glucose". *Radiology*, 179: 765-770 (1991).
- [4] Wahl RL, Zasadny K, Helvie M, Hutchings GD, Weber B, Cody R. "Metabolic Monitoring of Breast Cancer Chemohomotherapy using Position Emission Tomography: Initial Evaluation", *J. Clin. Oncol.* 11:2101-2111 (1993).
- [5] Nieweg OE, Wong WH, Singletary SE, Hortobagyi GN, Kim EE. "Positron Emission Tomography of Glucose Metabolism in Breast Cancer. Potential for Tumor Detection, Staging, and Evaluation of Chemotherapy." *Ann. Acad. Sci.* 698: 423-428 (1993).
- [6] Moon DH, Hoh CK, Silverman DS, Glaspy JA, Phelps ME, Maddahi J. "Accuracy of Whole-body FDG PET for the Detection of Recurrent or Metastatic Breast Carcinoma." *J. Nucl. Med.* 37:99P (Abstract) (1996).
- [7] Adler LP, Crowe JP, al-Kaisi NK, Sunshine JL "Evaluation of Breast Masses and Axillary Lymph Nodes with [F-18]2-deoxy-2-fluoro-D-glucose PET" *Radiology* 187:743-750 (1993).
- [8] Wahl RL, Helvie MA, Chang AE, Andersson I, "Detection of Breast Cancer in Women after Augmentative Mammoplasty using Fluorine-18-fluorodeoxyglucose PET". *J. Nucl Med* 35:872-875 (1994)
- [9] Mintun M, Welch M, Siegel B, "Breast Cancer: PET Imaging of Estrogen Receptors". *Radiology*, 169, 45-48 (1988).
- [10] Dehdashti F, McGuire A, Van Broclin H, Seigel B, Andriole D, Griffeth L, Pomper M, Katzenellenbogen J, Welch M, "Assessment of 21-[18F]Fluoro-16(alpha)-Ethyl-19-Norprogesterone as a positron-emitting radiopharmaceutical for the detection of progesterin receptors in human breast carcinomas". *J. Nucl. Med.* 32, 1532-1537 (1991).
- [11] Flanagan FL, Dehdashti F, Mortimer JE, Siegel BA, Jonson S and Welch MJ, "PET Assessment of Response to Tamoxifen Therapy in Patients with Suspicion of Breast Cancer". *J. Nucl. Med.* 37:99P (Abstract) (1996).
- [12] Katz D, "Scintimammography: Magic Bullet or False Promise?" *J.Nucl. Med.*36:15-20(1995).
- [13] Thompson CJ, Murth K, Weinberg IN, Mako F, "Feasibility Study for Positron Emission Mammography", *Med. Phys.* 1994 21:529-538.
- [14] Freifelder R and Karp JS, "A Dedicated PET Scanner for Breast Cancer", *IEEE 1995 Med. Imag. Conf. Proc.* 1358-1362 (1995).
- [15] Huchins GD, Simon AJ "Evaluation of Prototype Geometries for Breast Imaging with PET Radiopharmaceuticals", *J. Nucl. Med.* 36 69P (Abstract) (1995).
- [16] Moses WW, Budinger TF, Huesman RH, Derenzo SE "PET Camera Designs for Imaging Breast Cancer and Axillary Node Involvement", *J. Nucl. Med.* 36, 69P (Abstract) (1995).
- [17] Sandell A, Erlandsson K, Bertenstan L, "A Scanner for Positron Emission Mammography", *Eur. Conf. on Res. and App. of PET in Oncology*, p. 88-89 (1996).

DEVELOPMENT OF A HIGH-RESOLUTION PET DETECTOR USING LSO AND WAVELENGTH-SHIFTING FIBERS

William Worstell, Olof Johnson, and Valery Zawarzin
Boston University Physics Department
590 Commonwealth Avenue, Boston, MA 02215

Abstract

By using wavelength-shifting fibers coupled to thin plates of LSO and to photomultipliers, we have demonstrated spatial resolution of 2mm FWHM for photocapture events. Optimized systems are believed to be capable of better than 1mm FWHM resolution, without requiring either very small crystals or large numbers of photosensors. With this sensor resolution, annihilation acollinearity dominates system resolution for large PET rings. By radially stacking alternating layers of thin crystals and wavelength-shifting fibers, a direct depth-of-interaction measurement is possible. Energy measurements and coincidence timing may be provided by trigger photomultipliers in a dual-photodetector geometry. Results from computer simulations and component response measurements on proof-of-concept prototypes are presented.

I. INTRODUCTION

We are developing very high-precision PET detector modules with depth-of-interaction sensitivity, using a new design incorporating wavelength-shifting fiber readout of thin LSO crystals. By building modules from thin crystal layers stacked radially, one can obtain both depth-of-interaction information and fine spatial resolution in the tangential and axial directions. Component-level testing of this technique has demonstrated <2 mm FWHM spatial resolution for 2mm thick LSO crystals. Optimization and extrapolation to full PET systems may yield devices with resolution as small as 1mm FWHM using 1-2mm thick crystal layers; the resolution is expected to vary linearly with the crystal layer thickness. Depth-of-interaction sensitivity is essential for uniformly high-precision PET throughout a large field-of-view, if one is to preserve the detector thickness needed for high efficiency and high event statistics. Depth-of-interaction sensitivity also minimizes the necessary detector diameter, thereby decreasing both acollinearity errors and system costs, while increasing solid angle coverage. Our modular device design permits testing of a variety of detection geometries, including geometries appropriate for laboratory animal, human brain, and dedicated PET mammography applications.

II. MATERIALS AND METHODS

We have used ribbons of wavelength-shifting fibers to determine the positions of gamma-ray interactions within thin LSO scintillator crystals. Within a wavelength-shifting fiber, fluorescent dopant molecules absorb short-wavelength incident photons and then isotropically emit secondary longer-wavelength photons. One can use the fluorescent re-emission

process effectively to inject light into a light pipe through the sides of the pipe, since a fraction of the re-emitted light is trapped and piped along the fiber. In this way, the fiber becomes a light sensor, with short-wavelength light as input and long-wavelength light as output. An array of parallel fibers (i.e. a fiber ribbon) may then be used to measure incident light profiles in one dimension; two perpendicular ribbons (on opposite faces of the thinscintillator crystal) can provide a two-dimensional incident light profile measurement. Gamma-ray interactions in dense scintillators result in a very nearly point-like light source, because of the short range of secondary photocapture electrons. For polished high-index scintillator crystals, only light emerging nearly normal to the crystal surface escapes total internal reflection, resulting in an emission spot with diameter comparable to the crystal thickness. We earlier described this technique as applied to BGO crystals read out with red wavelength-shifting fibers [1].

In the present work we have focussed on the fast, high-Z, high-brightness scintillator Lutetium Oxyorthosilicate or LSO [2]. We have performed most of our initial measurements on two samples of LSO, each 2mm x 10mm x 10mm, which we obtained from Schlumberger-Doll Research [3]. These crystals were hand-polished on their large surfaces, and all surfaces not coupled to fibers were painted black. Fibers were coupled to crystals with a high-index epoxy ($n=1.65$), EpoTek OG127 [4]. For readout fibers we used 1-mm diameter, round, doubly-clad wavelength-shifting fibers from Kuraray Corp [5]; we obtained our best spectral matching with their spectral type Y-11. Doubly-clad fibers have a core refractive index of 1.60, an inner cladding index of 1.49, and an outer cladding index of 1.42; this yields a numerical aperture of 0.74 and a trapping efficiency of about 7% per fiber end for the re-emitted light (the remaining 86% of the re-emitted light is not trapped and emerges through the sides of the fiber ribbon).

Our initial tests have been carried out with the apparatus illustrated schematically in Figure 1. We form a pencil beam of 511-keV gamma rays by requiring the coincident detection of two back-to-back annihilation gammas produced by a nearly point-like Na-22 positron source. The first of the two gammas strikes a small 1mm x 3mm x 15mm LSO "triggering" crystal through its 1mm x 3mm entry face, while the partner ray goes through a 1mm lead collimator to the "target" 2mm x 10mm x 10mm crystal. The "target" crystal is coupled to a ribbon of 10 parallel 1mm diameter round wavelength-shifting fibers and to a trigger PMT. Since the light collected by the trigger PMT is proportional to the energy deposited in the target crystal, we are able to select events with photocapture of a pencil-beam gamma by the target crystal, by requiring a large trigger signal in coincidence with a signal from the "triggering" crystal. The "triggering"

LSO crystal and its PMT, the Na22 source and collimator are all mounted on a calibrated X-Y adjustable table, while the "target" crystal and PMT with fiber assembly are fixed; in this way, a pencil beam can be precisely directed into the "target" setup, and may be swept along the target. All measurements are made with unshaped signals directly coupled to charge-sensitive ADCs (LeCroy 2249W); the timing gate width was 150nsec and only photopeak events were used for analysis.

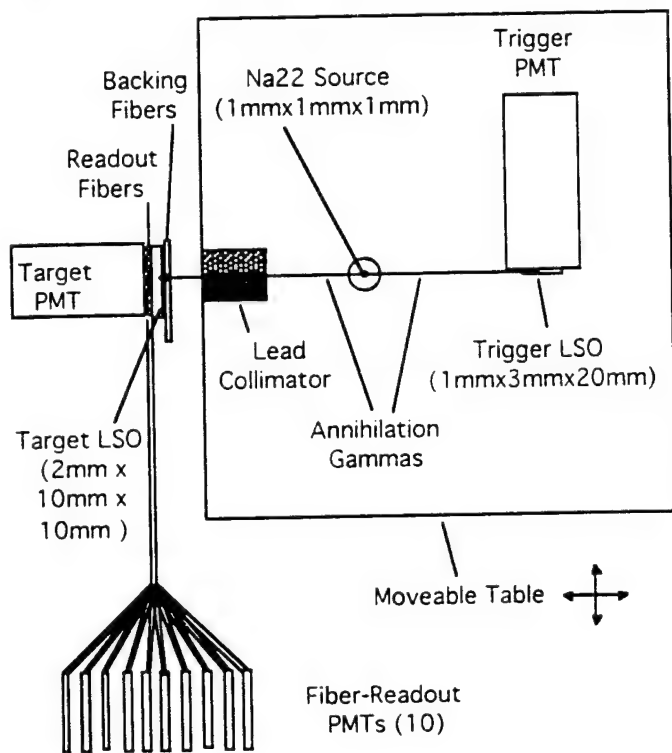


Figure 1: Schematic illustration of test apparatus.

Each of 10 fibers coupled to the target crystal is read out by an individual Hamamatsu R1635 PMT, allowing us to record the light profile and centroid position within the fiber ribbon on an event-by-event basis; all PMTs were calibrated and outputs converted to photoelectrons. The index of refraction of LSO is about 1.8, so we used the high-index optical epoxy for coupling crystals to fibers. The thin sides were blackened with an opaque mixture of high-index epoxy and xerographic toner (to simulate a larger crystal). Fibers were coupled to both of the large LSO surfaces, with 30cm long fibers having one polished end at the readout PMTs and their other ends 1 cm from the crystal. Light trapped at the optical interface between cladding and air ("cladding light") was removed by an opaque fiber holder gripping each fiber before its coupling to its readout PMT. The fiber/PMT optical interface was made with optical grease.

We have developed a complete Monte Carlo simulation of our detector's optics, including all optical interfaces and the correct geometry for round multiclad fibers. We have also developed a detailed radiation transport Monte Carlo simulation to study the effects of gamma-ray scattering and attenuation both in objects being imaged and within the detector itself. The latter simulation is based on the GEANT detector simulation code commonly used in high-energy

physics, which allows for simple implementation and modifications of the detector geometry through a flexible and powerful user interface. We generate gamma-rays from our source phantom according to a positron range distribution appropriate to ^{18}F , and with acollinearity between the annihilation gammas sampled from a Gaussian distribution with width 0.3 degrees. The detector resolution was usually taken to match the (not-yet-optimized) response functions measured with our test apparatus, and matches the measured dependence on light yield (gamma ray energy).

We have also begun work on making images with simulated data using a simple 2-D filtered back-projection reconstruction algorithm, for a number of test phantoms. In particular, we have looked at the benefits of depth-of-interaction resolution for small-diameter systems such as for use with laboratory animals. For some of these studies we have simulated a 1/2-scale version of a standard resolution phantom, with resulting 10cm diameter axially symmetric phantom viewed by a simulated 20cm diameter detector ring. To contrast with our detector, we have modelled a device without depth-of-interaction sensitivity, consisting of 8mm thick LSO on a 20cm diameter ring. For the radially-segmented fiber readout 20cm diameter ring we have used a total crystal thickness of 24mm, which would result in improve coincident efficiency by a factor of 3.2 relative to a 8mm thickness ring.

A wide range of system design options are open with a radially-segmented fiber readout geometry, and we have begun our exploration of these options with a baseline module having thickness 24mm and area 128mm x 128mm. Our plan is to construct and test at least one such module within the coming year. Assuming 2mm thick LSO layers and 1mm diameter fibers, this requires the readout of $13 \times 128 = 1664$ fibers per module. Multiplexing is clearly necessary in order minimize the cost for readout photomultipliers and digitizing electronics. One method for such multiplexing, employing separate readout of two fiber ends, is illustrated schematically in Figure 2 below. Other schemes, including mirrored fibers and two different colors of waveshifting fiber, are possible.

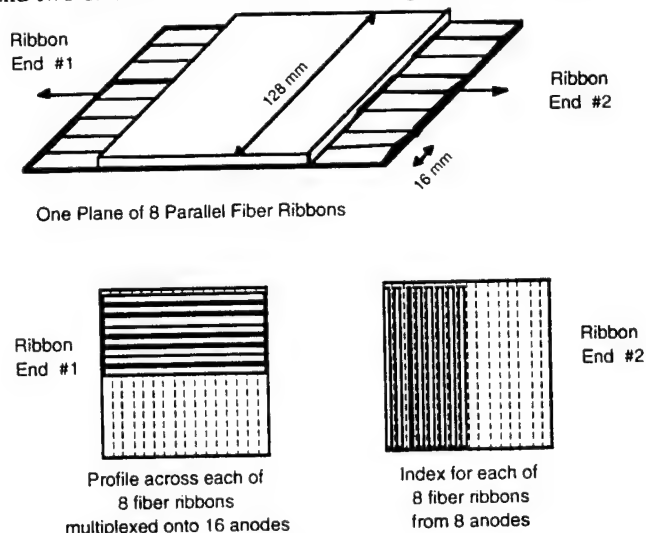


Figure 2: Multiplexed readout of fiber Ribbons using 16-channel multianode photomultipliers.

We have been testing a new R5800-L16 multianode photomultiplier from Hamamatsu Corporation, which combines 16 input pixels each 1mm x 16mm in area with a very narrow pulses (2ns FWHM) and good single-photoelectron resolution [6]. By reading out the two ends of multiclad fiber ribbons to two different multianode PMTs, one can read out as many as 256 fiber ends per PMT. Multiplexed readout of fiber ribbons corresponding to different crystal layers is also possible and probably desirable. If 0.5mm-diameter fibers are used, the physical limit is 1000 fiber ends per PMT. Although not indicated in the figure, it may be desirable to break up each 128mm x 128mm crystal plane into 64 16mm x 16mm optically isolated "cells" to reduce multiplexing cross-talk.

Electronics channel count can be minimized by charge-division readout (two signals rather than 16 from each photomultiplier) as is typically done with crossed-wire position sensitive PMTs. We have measured 20ns pulse widths (into a 50 ohm load) and $\ll 1$ mm resolution at 20 photoelectrons for charge division readout of our R5800-L16 PMT, using 100 ohm resistors to connect the anodes. In principle, the readout of a 16-layer module with area 128 mm x 128mm using 0.5mm fibers could require just 4 multianode photomultipliers (at a current cost of \$1500 each), with 8 associated fast ADC channels.

III. PRELIMINARY RESULTS

Our measured light yield for fiber readout of LSO crystals is in general agreement with our expectations. The light output for LSO is quoted at various levels in the literature, and is a strong function of the concentration of Cerium dopant: the most recent work cites a light yield of 20,000 photons/MeV deposited or about 10,000 photons per annihilation gamma photocapture event for LSO with a Cerium concentration of 0.22% [7]. Monte Carlo simulations predict that more than 25% of emitted photons should emerge from a given crystal readout face into the corresponding fiber ribbon, with photons incident at large angles (relative to the surface normal) totally internally reflected. Direct coupling of a photomultiplier with 20% quantum efficiency (when averaged over the LSO spectrum) to LSO with this brightness should thus give about 500 photoelectrons: this is consistent with our measured light yield in this "direct coupled" geometry. The next link in the optical chain is the match of the emission spectrum of the LSO crystal to the absorption spectrum of the fiber. This factor is about 60%, based on convolution of published LSO emission spectra and Kuraray's absorption spectra for Y-11. We thus expect that roughly 1500 scintillation photons are absorbed and re-emitted within the wavelength shifting fibers in each photocapture event.

Multiclad fibers trap 14% of their re-emitted light, or 7% per fiber end. Our measurements comparing light yield with multiclad vs. singly clad fibers, where the latter have 4% trapping per end, confirms this trapping fraction for the multiclad fibers we used. This implies that with multiclad fibers about 100 photons are piped toward each fiber end each photocapture event. Finally, some photons were attenuated within the readout fibers (such self-absorption filters out the

shortest-wavelength photons, and typically results in re-emission of an unpiped green photon), and a few photons arriving at the photomultiplier were reflected at the optical interface between fiber and photomultiplier. Our estimates of these effects were that we had about 80 photons entering our fiber readout photomultipliers each photocapture event, where they had an average quantum efficiency of about 10% for being converted to photoelectrons (Y-11 has its emission peak at 495 nm). This accounts for the roughly 8 photoelectrons which we observed per photocapture event with our test apparatus. This light yield, although small, is sufficient for multiplexed readout with good efficiency. Additional light yield may be achievable by using fibers with a better spectral match to LSO emission, by using PMTs with better quantum efficiency for green light (green-extended R5800-L16 PMTs are currently under development at Hamamatsu) or by obtaining brighter LSO.

The emission light profile from LSO crystals and the measured spatial resolution achieved at our current light level is shown in Figure 3 below. The resolution horizontal scale has been calibrated by moving the pencil beam in our test fixture across the crystal by known increments and measuring the resulting changes in the measured centroid position.

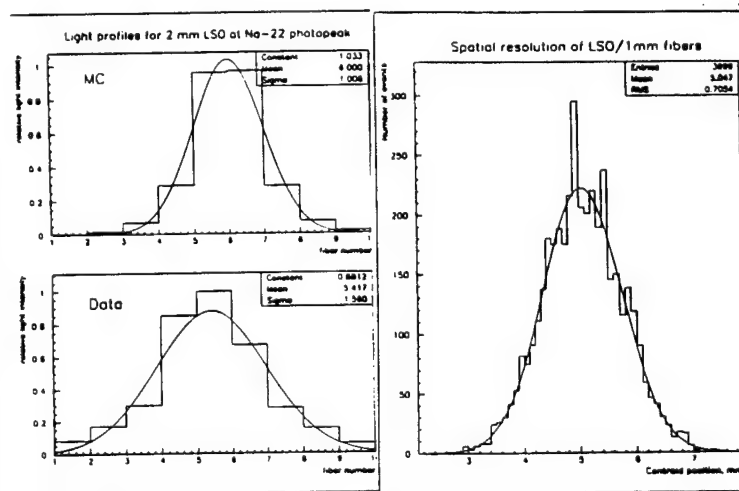


Figure 3: Measured response of LSO/Fiber test apparatus.

Left = Predicted and measured profile of light collection.
Right = Measured spatial resolution using centroids.

By measuring the distribution of photoelectrons across the fiber ribbon for photocapture events, we were able to reconstruct the event position with an accuracy of about 0.7mm RMS. There is still a contribution from the beam width to this resolution, for which we have not corrected. The accuracy of our coordinate measurement varies directly with the width of the light emission profile, so that the quality of crystal surface finish is important. Our Monte Carlo optical simulation predicted a profile of about 1.0mm RMS for a 2mm thick ideally polished LSO crystal, while the measured profile had a width of 1.6mm RMS. Evidently, our crystal surface preparation and fiber coupling could be improved. Spatial resolution improves with light yield like the square root of the number of photoelectrons N , and ideally the resolution should approach the profile width / \sqrt{N} .

We have carried out a simulation for a geometry appropriate to Positron-Emission Mammography, which we have simplified as two parallel planes separated by 10cm of water. Figure 4 illustrates the line-spread function (LSF) predicted for a perfect detector (due to just positron range and acollinearity), for fiber readout from 1mm thick LSO, and for fiber readout from 2mm thick LSO; the latter two are extrapolated from our non-optimized test results. It is apparent that range and acollinearity effects are very small.

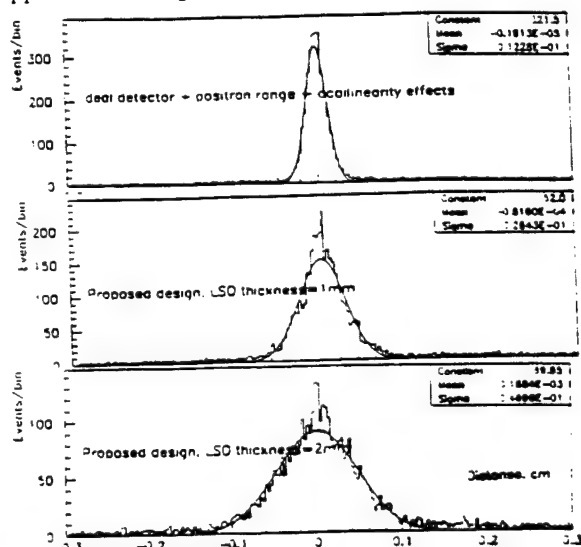


Figure 4: Simulated line-spread function and intrinsic limits.

As mentioned earlier, we have contrasted the simulated response of our proposed detector with that of a device with comparable spatial resolution but without depth-of-interaction sensitivity; both were formed into 20cm diameter rings.

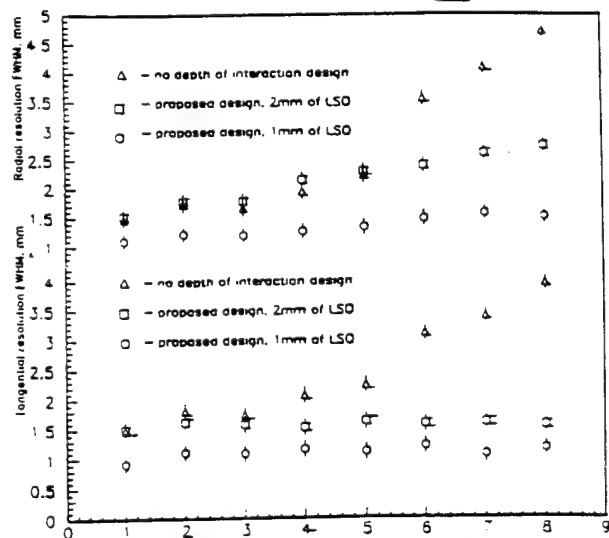


Figure 5: Resolution vs. radial position.
TOP = No DOI, MID = 2mm/ fiber, BOT = 1mm/ fiber

Figure 5 shows the reconstructed resolution as a function of distance from the center of the field-of-view for each device. Again, we have used the measured but not-yet-optimized resolution from our test apparatus as input to this simulation; in addition, we have indicated the resolution which should be achievable with 1mm thick LSO layers with

our fiber readout. While our device has very nearly uniform resolution over the entire field of view, the device without depth-of-interaction sensitivity has clear resolution degradation away from the center of the field of view.

IV. DISCUSSION

Radially segmented readout of thin LSO crystals with wavelength-shifting fibers has the following advantages:

- Very High Spatial Resolution
- Depth-of-Interaction Measurement
- High Rate Capability
- Potential for Low Cost
- Flexible Readout Options

Unlike most designs for very high-resolution PET detectors, this design scales readily to large systems while preserving high efficiency and fine resolution; it also only makes use of existing photosensor and electronics technology.

Since the spatial resolution scales linearly with the crystal thickness, extremely fine spatial resolution should be achievable with small-diameter rings. Resolution blurring due to acollinearity (about 2.2mm FWHM per meter of ring diameter) can be made to dominate system resolution for large rings; smaller rings can achieve submillimeter resolution with high efficiency across a large field of view (if short-range positrons like 18F are used) by using very thin crystal layers. Axial resolution is naturally comparable to tangential resolution, and to depth-of-interaction resolution. Double-hits from Compton-scatters within the detector (which can degrade resolution of block detectors) are readily identifiable with suitable electronics, since they will almost always deposit energy in more than one crystal layer. Use may be made of Compton scattered (rather than photocaptured) events in small rings imaging objects with little scatter, with only a small degradation in spatial resolution. Finally, detector modules may be combined in a "gapless" geometry by radially overlapping in a pinwheel arrangement as shown in Figure 5; any oversampling which results in the overlap regions may be corrected using depth-of-interaction information.

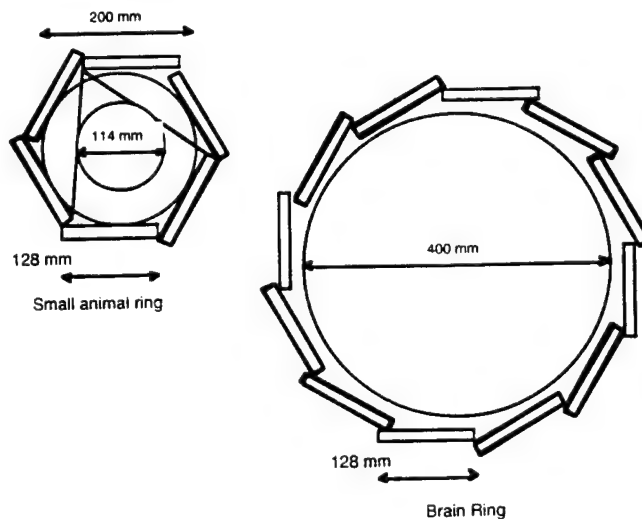


Figure 5: Conceptual System Geometries with Fiber Readout

Depth-of-interaction measurement is critical for preserving very fine spatial resolution throughout a large field of view, without compromising on detector coincidence efficiency (which is critical for the statistics needed to make a high-resolution image). Depth-of-interaction sensitivity permits a reduction in ring diameter, which pays several dividends: lower system costs for less scintillator and fewer readout channels, smaller effects from acollinearity, and higher efficiency through greater solid angle coverage. The last comes at the price of increased scatter acceptance, but this trade-off is already being chosen in the selection of 3-D over 2-D PET. Increasing the module size (both in axial and tangential dimension) yields a more cost-effective readout by using longer readout fibers, which increases the detector volume/PMT area ratio; the price paid is lower rate capability.

With fully multiplexed readout (including in depth) of 128mm x 128mm area modules, a rate capability of >1Mhz/module should be achievable. The 45ns decay time of LSO permits signal integration over 150ns, with digitization of charge-division signals to the required 7-bit resolution possible in less than 1 microsecond. Time correspondence of 8 PE signals from 45ns scintillator has high efficiency within a 10-20ns window. The coincidence timing (for singles rejection) and energy resolution achievable with an all-fiber readout are more problematic. If necessary, fiber readout can be supplemented with large trigger PMTs which would collect the re-emitted but non-trapped light which emerges through the sides of the wavelength-shifting fibers and to which both fibers and crystals are transparent. Our measurements have shown that although less than 10% of LSO light passing through one fiber layer is absorbed in the next, the layers which are opaque to LSO light are very transparent to fiber light. Supplemental readout with large trigger PMTs would yield hundreds of photoelectrons, sufficient for 1ns coincidences and energy resolution limited by effects other than photostatistics. Large-area photodiodes might be substituted for photomultipliers to preserve compatibility with operation in a magnetic field, if necessary.

Fiber readout of LSO is potentially quite cost-effective, presuming that the bulk price of LSO continues to fall. It is currently at \$50/cc in quantities of 100's of cc's, and is projected by the crystal grower to fall to \$15/cc in about 1 year. At this price it becomes competitive with BGO, and fiber cutting and polishing costs become significant (especially for very high-resolution devices with small crystals). The crystal cutting and polishing required for the thin flat crystals used with fiber readout is significantly less than for the long thin crystals in other detectors, and we will carefully check how our performance varies with crystal surface treatment. The cost for 4 multianode PMTs to read out fibers from a 128mm x 128mm module is comparable to the 25 1" PMTs which would be required to read out the same area in a block detector; if larger modules have sufficient rate capability, fiber readout costs fall still further. The cost of fibers in quantity, about \$1/m for 0.5mm diameter, makes the fiber cost small in comparison to crystals and PMTs. Finally, the electronics channel count reduction yields savings, reducing the 25 ADCs for the above block detector to 8 in our design.

Although our initial results have been encouraging, we have been somewhat handicapped by the availability of only small samples of LSO. This situation has now changed, and we anticipate the availability of hundreds of cc's of LSO by early 1996. Our plan is to further optimize and to construct large modules with this new material as soon as possible.

V. CONCLUSIONS

We have demonstrated that wavelength-shifting fibers can be used to read out gamma-ray interaction positions within thin sheets of LSO crystals, with high efficiency. The spatial resolution achievable (FWHM) is less than the thickness of the crystal layer being read out. Consequently, by constructing a detector from a thick stack of many thin layers, one can combine very fine spatial resolution with depth of interaction sensitivity and high efficiency. With optical multiplexing at the crystal layers and at the readout photomultipliers, a cost-effective design with extremely high spatial resolution is achievable; this design is readily scaled to large-diameter systems. During the coming year, we plan to construct one or more 128mm x 128mm x 20mm thick modules to test and optimize this design.

ACKNOWLEDGMENTS

We would like to thank Dr. Charles Melcher of Schlumberger-Doll Research, for providing us with LSO samples, and to thank Kuraray Corporation for providing us with samples of their Y-11 multicladd wavelength shifting fiber. We are grateful to Hamamatsu Corporation for the loan of a R5800-L16 multianode PMT which was used in this work. We would also like to thank Charles Burnham of Massachusetts General Hospital for many helpful discussions regarding PET systems. This work was supported through the Boston University Center for Photonics Research, under Grant No. N00014-93-1-1186 from the Office of Naval Research.

REFERENCES

- 1 W. Worstell, S. Doulas, O. Johnson, C. Lin, "Scintillator Crystal Readout with Wavelength-Shifting Optical Fibers," IEEE Medical Imaging Conference Proceedings, 1994.
- 2 C.L.Melcher and J.S.Schweitzer: "Cerium-doped lutetium orthosilicate: A fast, efficient new scintillator", IEEE Trans. Nucl. Sci. NS-39, pp. 502-504, 1992
- 3 Schlumberger-Doll Research, CT
- 4 Epotek Corp., Billerica, MA
- 5 Kuraray Corp., 200 Park Ave., New York, NY 1016
- 6 Hamamatsu Photonics, 360 Foothill Road, Bridgewater, NJ 08807
- 7 T. Ludziejewski et. al. "Advantages and Limitations of LSO Scintillator in Nuclear Physics Experiments", IEEE Trans. Nucl. Sci 42 Pg 328-336

Characterization of a new multianode PMT for low-level optical fiber readout*

D. Grigoriev¹, O. Johnson², W. Worstell², V. Zavarzin³

¹Budker Institute of Nuclear Physics, pr. Lavrentieva 11, Novosibirsk 630090, Russia

²Boston University Department of Physics, 590 Commonwealth av., Boston MA 02215

³Budker Institute of nuclear physics, Novosibirsk, Russia, currently at Boston University

Abstract

We have characterized the new Hamamatsu R5900-L16 multianode photomultiplier with regard to its suitability for position-sensitive readout with just two analog channels for each 16-anode PMT. Because of the low capacitance of the anode structure of the PMT, we obtain an output pulse width of less than 20 ns for narrow input pulses. We were able to obtain position-sensitive readout of single photoelectron pulses with a spatial width of less than 1 mm FWHM for a collimated light source and about 2 mm FWHM for single fiber. Combined with the good single photoelectron peak for R5900-L16, this provides excellent performance at very low light levels. We discuss application of this device to the precise determination of gamma-ray interaction position within thin crystal scintillators.

I. INTRODUCTION

Position sensitive photomultipliers have been used by a number of groups for the readout of scintillating or wavelength-shifting fibers. Crossed-wire and multianode PMTs have also been used for the position-sensitive readout of extended light sources [2-5]. At low light levels, the cross-talks within the PMT can result in significant degradation in spatial resolution. There are several sources of such cross-talks: light spreading through the entry window glass on the way to the photocathode, imperfect electron optics between photocathode and dynode structure, secondary electron shower spreading within the multiplier assembly, or just electrical cross-talks between anodes (induced signals). A significant difference between position-sensitive cross-wired PMTs like the Hamamatsu R2486, versus multianode PMTs like the Hamamatsu R4760, is the considerably higher cross-talks and therefore decreased spatial resolution at low light level of the former. The Hamamatsu R2486 for instance requires 10000 photons at 490 nm (about 1000 photoelectrons) to obtain a spatial resolution of 0.2 mm FWHM [2]; the resolution is proportional to the square root of the number of photoelectron per event. Another difficulty with cross-wired PMTs for some applications is its limited rate capability due to significant pulse width with typical resistor chain readout.

Nonetheless, the reduced electronics channel count and lower device cost (particularly per unit of useful photocathode area) associated with crossed-wire PMTs have made them attractive for several applications, including for the readout of sets of scintillating fibers.

There is some success in attempts to use charge division method for two-dimensional readout of an array of optical fibers by multianode PMT having just four analog channels [5]. But again, one needs hundreds of photons to obtain submillimeter resolution.

We investigated the properties of the newly developed PMT - the Hamamatsu R5900-L16 - because of its very promising specifications caused mainly by recently developed microchannel dynode structure.

II. EXPERIMENTAL SETUP

A. R5900-L16 - multianode PMT

The photomultiplier described here has external dimensions of merely a cube 25*25*25 mm. It has flat bialkali photocathode, 10-stage dynode structure and 16 anode stripes 0.8 * 16 mm regularly spaced at 1 mm pitch. An important feature of the PMT distinguishing it from previous ones is that the microchannel dynodes work effectively like separate PMTs in terms of electron optics. This minimizes electron shower smearing and allows one to obtain very fine spatial resolution as will be shown below. Another useful feature of the microchannel structure is a relatively high gain at low operating voltage - about $3.4 \cdot 10^6$ at 800V. The first prototype of R5900-L16 sent to us by Hamamatsu had a size of photocathode of 15.5 * 15.5 mm which is a 0.5mm narrower than dynode structure. Most of the measurements were done on this particular PMT. The photocathode size of the last version of R5900-L16 is significantly larger - approximately 21 * 22 mm. We have repeated some of the measurements to check the impact of this design change on the performance.

B. Charge Division Readout

We have connected 16 anodes of the PMT by a linear array of 15 100-ohm resistors to couple 16 individual outputs into 2 charge division outputs. Each of the two signals was directly coupled through 50-ohm cables to a LeCroy 2249W operating with a 150 ns gate width. To minimize artifacts caused by discrete nature of ADC data we have inserted 10-fold

*This work was supported through the Boston University Center for Photonics Research, under Grant No. 00014-93-1186 from the Office of Naval Research.

amplification of the charge division signals giving us a single photoelectron peak at about 35 channels of the ADC over the pedestal.

B. Data Acquisition System

For measurements described here we used rather simple data acquisition system consisting of a CAMAC ADC mentioned above and micro-VAX computer under Open VMS connected to the CAMAC crate and controller via SCSI-bus. Data collected on a disk of the computer then were analyzed in PAW (CERN written data analysis software) session.

III. TESTS AND MEASUREMENTS

A. Timing and Single Photoelectron Characteristics

The PMT itself (when its anodes are read out separately) has fast rise time and narrow pulse width - 0.6 ns rise time, 1.7 ns fall time when loaded to 50 Ohm. After connecting all anodes by a linear array of 100-Ohm resistors, we obtain a pulse width of less than 20 ns. To check single photoelectron amplitude peak we connected together two ends of the charge division chain. The PMT was illuminated by a green LED giving 0.1 photoelectron in average. The distribution is shown on Fig. 1. The peak-to-valley ratio of almost 3:1 is a very desirable characteristic for low light level applications.

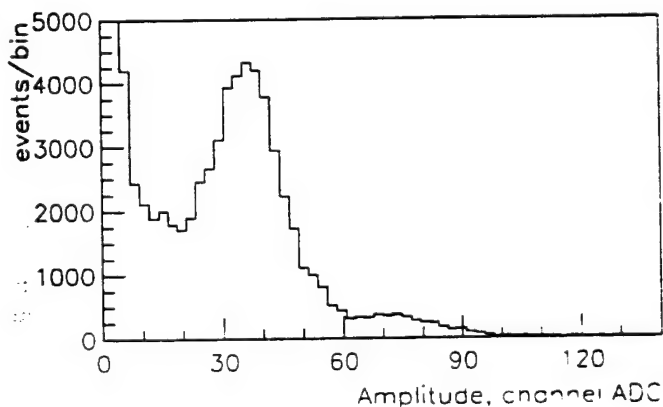


Figure 1: Single photoelectron peak of the R5900-L16. All anodes are read out together. HV=800V.

B. Charge Division Calibration

Ideally, if we know parameters of the chain - we can calculate the calibration coefficient between charge division ratio $R = (A_2 - A_1) / (A_1 + A_2)$ (A_1 and A_2 - amplitudes measured from two ends of the chain) and position in the chain, considering each anode to be a current source. The correspondence between charge division node number and measured ratio R should be linear. Therefore even if several photoelectrons are distributed over several PMT anodes the measured ratio R would correspond to the center-of-gravity of

received photoelectrons. In our particular case we have $R_{in} = 50$ Ohm and 15 resistor of the chain 100 Ohm each. So ideally for point source from the first or the last anode we should measure the ratio

$$R = \pm (50 + 15 \cdot 100 - 50) / (50 + 15 \cdot 100 + 50) = \pm 0.9375.$$

In real situation one has to correct this ratio for different gains and input impedances of the two amplifiers. Practically we found that the ratio R ranges from -1.05 to 1.05, which means that anodes others than illuminated by light source produce induced signals of inverse polarity. Indeed we have seen and measured such signals on the scope - the sum of all anodes but illuminated one gives approximately 15% of the main signal. Neglecting the fact of induced signals we could calculate the linear coefficient for conversion of the measured ratio R to the signal center-of-gravity position:

$$K = 15 / (1.05 - (-1.05)) = 7.14,$$

where 15mm - separation between the first and the last anodes. Using this coefficient we have plotted then center-of-gravity coordinate versus actual position of the light source. The plot and linear fit of the data are shown on Fig.2.

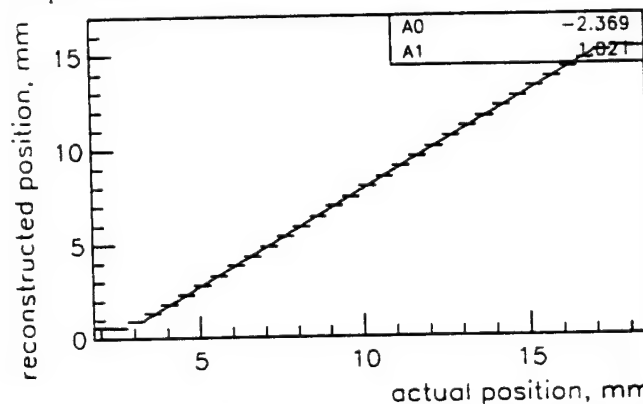


Figure 2: Reconstructed coordinate linearity. A 0.5 mm fiber coupled to a green LED was positioned by a calibrated translation stage with an increment of 0.5 mm. At each position corresponding charge division coordinate was calculated and plotted. Light level is approximately 100 photoelectrons.

C. Intrinsic Spatial Resolution of the PMT

In order to measure intrinsic resolution of the PMT we have used collimated parallel light beam produced by a green LED and a black shield with two holes of 0.3mm diameter. The shield was mounted directly on the PMT window so we were able to avoid light spreading in the window glass which thickness is about 1.5 mm. The LED intensity was adjusted to give about 0.1 photoelectrons per pulse. Only events corresponding to single photoelectron peak were recorded therefore converted photon should have coordinate of the first or the second hole of the collimator. The distribution and two-gaussian fit are shown on Fig.3. The reconstructed distance between two peaks well matches the hole separation of 1mm. The width of each of the two peaks is about 0.25mm RMS (or 0.6mm FWHM).

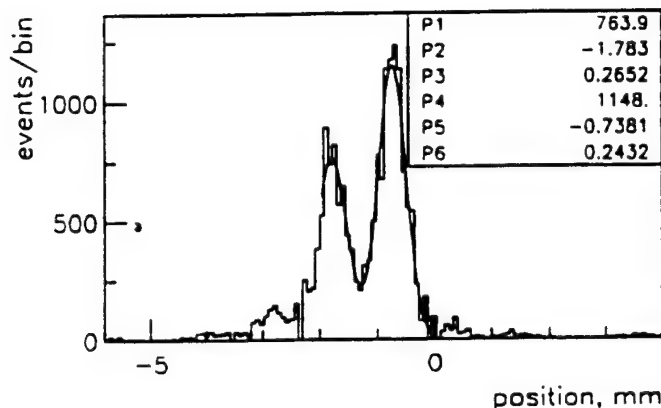


Figure 3: Reconstructed coordinate distribution for events selected around single-photoelectron peak ± 1 RMS. Light source is a double beam produced by green LED through a collimator - black film with two holes of 0.3 mm diameter separated by 1 mm. Two peaks clearly separated at a distance of about 1 mm.

D. Single Fiber Response

There are two difference between collimated beam and light coming from a fiber. First, fiber photons leave the surface of the fiber uniformly over the its cross-section. Second, these photons have an angular spreading of about 20-30 degrees, depending on type of the core and the cladding materials. These two factors together broaden the distribution of the photons converted on the photocathode. In order to evaluate this effect we have repeated previous measurement using instead of the collimated light beam - 0.5mm clear fiber coupled to a green LED and to the PMT by optical grease. The distribution is shown on Fig.4. It doesn't much differ from the distribution on Fig.3, which means that photoelectrons in this particular test are mostly distributed over two anodes or within 2 mm in physical space. Another useful test is how the resolution depends on number of registered photoelectrons. We found that the spatial resolution scales with the inverse of the square root of the number of the photoelectrons to well in excess of 20 photoelectrons. The results for different light levels are shown on Fig.5.

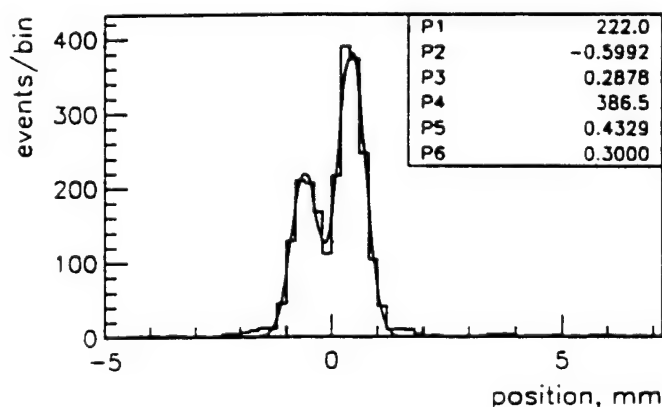


Figure 4: Reconstructed coordinate distribution for all events with amplitude greater than 0.5 photoelectron.. Light source is a green LED coupled to the PMT through a 0.5mm clear fiber giving an average of 0.1 photoelectron.

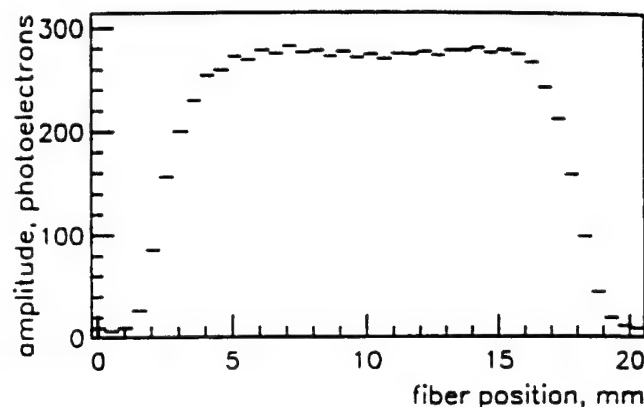


Figure 6: Visible light profile across the photocathode of the PMT. One end of a 0.5 mm fiber is coupled to a green LED, another end was moving in a proximity of the PMT face with a calibrated translation stage.

E. Field of view test.

All previous results were obtained in just few positions on the PMT window. Important questions also are how uniform and how big is field of view (photocathode area). Some edge effects are visible on Fig.2 so useful area for the first PMT tested was about 14*14mm. The result of a uniformity test is shown on Fig.6. The width of "uniform" area is about 15mm if one would agree to lose 50% of the signal. This lost would mean less number of photoelectrons registered and consequently some degradation in resolution on the edge.

As it was mentioned before, the last version of the PMT has wider active photocathode area. Therefore we have repeated the measurements reflected on Figs.2 and 6 and found that "useful" area of the last version of the PMT (based on the same criteria) is about 1mm wider in both directions (i.e. 16*16mm).

IV. DISCUSSION

We are particularly interested in application of this PMT to the readout of wavelength-shifting fibers coupled to thin layers of scintillator crystals, for use in a PET detector were designing [6]. In this application, the spread of the light across a ribbon of photomultiplier has a FWHM about equal to the thickness of the crystal - 2 mm for our device. Achievable spatial resolution limited by this spread could be in principle a FWHM of 2 mm divided by the square root of the number of photoelectrons measured. This resolution is then further degraded by the spatial resolution of the fiber readout PMT, which from the above measurements is about twice better.

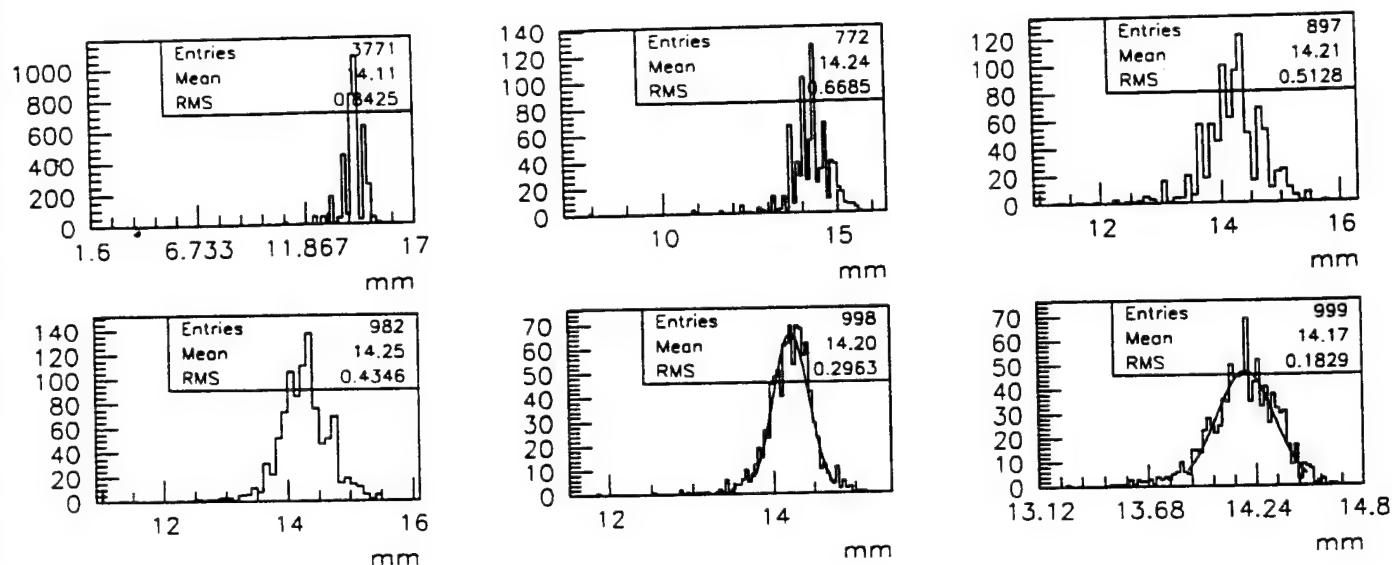


Figure 5: Reconstructed coordinate distribution for different light levels (upper row from left to the right: 1, 2 and 3 photoelectrons; bottom row from left to the right: 5, 10 and 20 photoelectrons). Light is coming from a green LED coupled to the PMT through a 0.5mm clear fiber.

Since the two effects are incoherent, we could preserve an intrinsic resolution of our crystal-fiber readout design undisturbed by the PMT itself. At a current cost of less than \$1500 in single-unit quantities, this PMT is cost-effective in comparison with competing devices, particularly in multiplexed geometries such as one obtains when reading out one end each of many fibers at each PMT anode input (e.g. 14 ribbons of 1mm-diameter fibers each 14mm wide, for total of 196 fibers, may be read out with just two PMTs by differing the orientation of the readout PMTs by 90 degrees about the fiber axis at the two fiber ends - presuming that just 1 fiber of the 196 fibers on a given event). The level of multiplexing possible at low light levels is critically dependent on the spatial resolution achievable.

V. CONCLUSION

We have studied the properties of a photomultiplier with charge division readout suitable for scintillating or wavelength-shifting fiber applications with submillimeter resolution at low light levels of just few photoelectrons. It was shown that intrinsic resolution of the PMT is better than 1mm FWHM even for single photoelectron signals. The spreading of the light coming from the fibers to the PMT windows deteriorates resolution greater than electron optics does. From the other hand we have found that electrical cross-talks between anodes don't disturb achievable resolution and linearity of the charge division method.

VI. ACKNOWLEDGMENTS

This authors wish to thank the staff of Hamamatsu Photonics K.K. for useful discussions and for their technical and production support.

VII. REFERENCES

- [1] Hamamatsu Photonics K. K., Electron Tube Center, 314-5 Shimokanzo, Toyoka village, Iwata-gun, Shizuoka-ken, 43801, Japan.
- [2] M. Salomon et al., "Fiber scintillators coupled to a multianode photomultiplier as a high rate tracking detector", *IEEE trans. Nucl. Sci.*, vol. NS-34(1), pp.525-527, 1987.
- [3] G. Comby et al., "Test of 64-channel PMT for imaging", *Nuclear Instruments and Methods*, vol. A269, pp.246-260, 1988.
- [4] J. Bahr et al., "Test of a position-sensitive photomultiplier for fast scintillating fiber detector read-out," *Nuclear Instruments and Methods*, vol. A330, pp.103-114, 1993.
- [5] S. Siegel et al., "Simple charge division readout for imaging scintillating arrays using a multi-channel PMT", *IEEE trans. Nucl. Sci.*, vol. 43(3), pp.1634-1641, 1996.
- [6] W. Worstell et al., "Development of a high resolution PET detector using LSO and wavelength-shifting fibers", *1995 IEEE Nucl. Sci and Med. Imaging Conf. Record*, vol. 3, pp. 1756-1760, 1995

Monte Carlo-based Implementation of the ML-EM Algorithm for 3-D PET Reconstruction¹

W. Worstell, H. Kudrolli, and V. Zavarzin

Boston University Physics Department and

Center for Photonics Research

590 Commonwealth Ave., Boston, MA 02215

Abstract

The Maximum Likelihood/Expectation Maximization algorithm for 3-D image reconstruction has the advantages of good noise properties for low-statistics data, good normalization, and flexibility in detector geometry. However, the ML-EM algorithm entails a considerable computational burden relative to Fourier-based techniques. We have been studying an implementation of the ML-EM algorithm which applies Monte Carlo event generation as an implicit use of the system matrix, rather than calculating system matrix elements explicitly. In addition to its speed and simplicity, this approach has additional advantages for high-resolution systems with very large numbers of lines-of-response. We present results and computation times for reconstructions of several software phantoms.

I. INTRODUCTION

The Maximum Likelihood/Expectation Maximization algorithm has been applied to positron emission tomography for many years [1-3], and is perhaps the most popular iterative reconstruction technique currently used in PET. Recently, several groups have implemented the EM algorithm for 3D PET reconstruction [4-6], with each such implementation resulting in considerable computational burden and coding complexity. One such calculation required 55 minutes on a 32-processor supercomputer *per iteration* to reconstruct 35 planes, with a typical reconstruction requiring of order 100 iterations. Although a speed-up by a factor as large as 50 may be possible by applying the method of ordered subsets [7], the fundamental difficulty of an extremely large system response matrix remains. The number of elements in this system matrix is equal to the product of the number of lines-of-response times the number of image voxels; both become very large in high-resolution 3-D systems. In what follows we will describe an Inverse Monte Carlo implementation of the ML/EM algorithm for 3D PET reconstruction which required 15 minutes on a single-processor workstation *per iteration* to reconstruct 32 planes containing 10 million events, and which converges in about 20 iterations. This speed-up is the result of statistically sampling from system matrix elements, rather than explicitly calculating them, during the reconstruction process.

Our interest in this problem arises from the reconstruction requirements for a high-resolution dual-plane detector with

restricted angular acceptance (a PET mammograph) [8]. For high-resolution systems operating in 3D mode, the number of distinguishable lines-of-response can exceed the number of events collected in a typical scan. Several groups have developed reconstruction algorithm for such systems based on backprojection filtering rather than filtered backprojection; in the former method one first backprojects event-by-event, then applies a 3D filter to deconvolve the point-spread-function of the backprojection operation from the image [9-12]. Several groups have been developing dedicated hardware for high-speed reconstruction using backprojection filtering [13-14]; in what follows we will similarly be backprojecting coincidence data into a backprojection image array at the outset of our reconstruction procedure.

An iterative reconstruction algorithm which uses the back-projected data image as input has been developed previously by other authors and termed the "Image Space Reconstruction Algorithm" or ISRA[15]. The ISRA method iteratively modifies a hypothesized source distribution so as to minimize the differences between the back-projection of forward-projected data from this hypothesized source, vs. the backprojection of actual measured data. This procedure has the advantage of greatly reducing the size of the arrays needed in the reconstruction, since one need save only the three-dimensional back-projection voxel array rather than arrays of measured and calculated projections onto lines-of-response. As presented by its authors, the ISRA does not converge to the maximum likelihood solution, and is not equivalent to ML/EM. Like ISRA, our reconstruction technique will compare the backprojection of forward-projected events which would be produced by a hypothesized source distribution with the backprojection of actual data events; unlike ISRA, our method is readily extended to achieve formal equivalence with ML/EM in the limit of large event statistics.

An important feature of ISRA as it was implemented by its authors is that it does not require explicit calculation of the system response matrix; this matrix contains the probabilities for events emitted from each of the source pixels to be assigned to each of the line-of-response projections. Instead, these probabilities were determined implicitly by forward-projecting rays from an iteratively updated image estimate volume onto the coincidence detector geometry, and then back-projecting rays from each detector element pair onto a back-projection image. In this way, the steps taken to obtain the comparison back-projection image from the hypothesized source distribution model the process of obtaining the data back-projection image from the real object. Our method preserves this modelling of the data collection during the reconstruction procedure, but it is more economical in its application of the forward- and back-projection steps

¹This work was supported by the U.S. Office of Naval Research under Grant No. N00014-93-1-1186 to the Boston University Center for Photonics Research.

connecting source voxels to back-projection image voxels. In ISRA an estimated image is forward-projected to obtain *calculated* projections on a view-by-view basis; in our Inverse Monte Carlo implementation *sample* forward-projection events are generated from the estimated image and their back-projections are accumulated. The extent of sampling required is dictated by the statistical accuracy of the projection dataset which is to be reconstructed.

Inverse Monte Carlo reconstruction has been advocated by other authors as offering a unified reconstruction framework for Emission Computed Tomography, providing simultaneous compensation for scatter, attenuation, and effects due to detector geometry and other detector attributes [16]. It has especially found advocates in SPECT, where the effects of scatter, attenuation, and detector/collimator geometry are more pronounced than in PET. However, the usual implementation of Inverse Monte Carlo has been simply to use Monte Carlo techniques to calculate the system response matrix, then to use this matrix in a conventional ML/EM reconstruction. Recently, Monte Carlo techniques have been advocated for scatter correction in 3D PET, in particular for whole-body scans [17-18]. These studies make use of an object-dependent attenuation and scatter model associated with a given emission dataset to generate the expected scatter contribution to the emission image, which is then subtracted. A second-order correction can then be applied to adjust for changes in the scatter distribution due to changes in the hypothesized source distribution after first-pass scatter subtraction. We propose an integrated approach (which we have not yet implemented) to scatter correction by building object-dependent scatter and attenuation into the Monte Carlo system response model used during our Inverse Monte Carlo reconstruction procedure. As with Monte Carlo event sampling generally, the number of Monte Carlo simulated scatter events required is only a few times the number of scatter events collected in a given dataset.

Thus far we have principally examined application of our method to noise-free data from software phantoms, without any contribution from attenuation or scatter effects. Our emphasis has been on determining the speed and convergence properties of this technique in its simplest form. In what follows we will first detail the principle and theory of Monte Carlo sampling in an iterative image space reconstruction algorithm, then will discuss our experience with a simple implementation operating on software phantom data, and finally will conclude with prospects for future application to scanner data from real objects and possible scatter correction techniques.

II. THEORY

A. Importance Sampling in ML/EM

One representation of the EM algorithm is given by:

$$\lambda_i^{(n+1)} = \lambda_i^{(n)} \cdot \sum_j P_{ij} \frac{y_j}{\sum_i P_{ij} \lambda_i^{(n)}}$$

where $\lambda_i^{(n)}$ gives the n th iteration of the i th voxel of the reconstructed distribution, y_j gives the j th projection (typically, events along the j th line-of-response), and P_{ji} gives

the probability that a photon emitted at i will be detected in projection j ; this last is the system response matrix. In a 3D EM reconstruction for a typical scanner geometry, this system matrix is much too large to store in memory; symmetries must be used in order to reduce a previously-calculated system matrix to a form which is stored on disk. For this reason true 3-D iterative reconstruction via EM/ML is much slower than in the 2-D case.

An examination of the above expression for the EM algorithm shows that an alternative approach is possible. In the conventional approach, the system matrix forward-projects the source estimate, voxel by voxel, according to the system response matrix; the corresponding term in the above expression is: $\sum P_{ij} \lambda_i^{(n)}$. This forward projection is accumulated over all voxel elements within the source distribution, accumulating the response to a distributed source by summing over the responses to individual source elements. An alternative method of forward projection is the Monte Carlo generation of events sampled from the source distribution, where the Monte Carlo model can support varying levels of detail regarding detector geometry, response, object and detector attenuation and scatter, etc.. The sequence with which source voxels contribute to Monte Carlo event generation is immaterial since the results are accumulated; one is also free to choose the total number of events generated, so long as the event production from each source voxel is proportional to the source distribution hypothesis $\lambda_i^{(n)}$.

While Monte Carlo event generation is often thought of as computationally intensive, in fact it can require much less calculation than the determination of system response matrix elements which cannot be stored in memory. Significantly, the effective precision with which the system matrix is calculated (sampled) is simply tuned to the event statistics of a given dataset, since *there is no point to calculating or applying the system matrix more accurately than it has been sampled in a given empirical measurement*. This criterion sets the maximum number of Monte Carlo events to be generated as no more than a few times the number of events collected by the scanner in the dataset which is to be reconstructed. Neglect of this criterion can lead to the false precision of "reconstructing" a source distribution which reproduces the statistical fluctuations in one's data as if it were significant information; this can happen with the conventional ML/EM implementation if it is continued through too many iterations.

In general, producing 10 times as many simulated events as actual events will make statistical fluctuations in the simulated data sufficiently small in comparison to statistical fluctuations in the actual data; this holds for such details as scatter and detector response variations as well as simple detector geometry effects. The critical point is the fidelity of the Monte Carlo system response model (which is incorporated in the Inverse Monte Carlo procedure) to the actual response of a physical device. In the software phantom studies discussed below the detector response model and Inverse Monte Carlo model are identical, corresponding to the most favorable case.

Table 1
Formal Analogy between Conventional ML/EM and Inverse MC ML/EM Algorithms

Expression	Significance	Conventional ML/EM	Inverse MC ML/EM
$\lambda_i^{(n)}$	n(th) iteration of reconstructed source distribution	3-D Matrix in real space	3-D Matrix in real space
P_{ij}	System response matrix / System response operator	i index: source voxels j index: lines-of-response	i index: source voxels j index: voxels in back-projection space
y_j	Measured event data	Accumulated data indexed by line-of-response	Back-projected measured data, indexed by voxel in back- projection space
$\sum_i P_{ij} \lambda_i^{(n)}$	Forward projection	Calculated inner product of system response matrix and source hypothesis matrix	Accumulated back-projections of Monte Carlo-generated events
$\frac{y_j}{\sum_i P_{ij} \lambda_i^{(n)}}$	Ratio calculation	Ratio observed to expected within each line-of-response	Ratio observed to expected within each back-projection space voxel
$\sum_j P_{ij} \frac{y_j}{\sum_i P_{ij} \lambda_i^{(n)}}$	Back projection	Calculated inner product of ratio matrix and system response matrix	Generate events and back- project into ratio space, to calculate weighted average ratio (see text discussion)
$\lambda_i^{(n+1)} = \lambda_i^{(n)} \cdot \sum_j P_{ij} \frac{y_j}{\sum_i P_{ij} \lambda_i^{(n)}}$	Update source hypothesis	By source voxel	By source voxel

B. Analogy between Conventional and Inverse Monte Carlo ML/EM Algorithm

In Table 1 we detail the correspondence between the symbols in the ML/EM algorithm expression as conventionally interpreted, and as interpreted in our Inverse Monte Carlo implementation. The intent throughout is to retain the purpose of the conventional formulation while substituting the means of the new formulation. We begin by detailing the correspondence between symbols in each of the two interpretations. In each case, the n-th iteration of the reconstructed source distribution is expressed as $\lambda_i^{(n)}$. In the conventional implementation the system matrix P_{ij} maps each voxel of the reconstructed data volume into its sinogram projection (indexed by line-of-response); in the Inverse Monte Carlo formulation, the system *projection operator* P_{ij} maps each voxel of the reconstructed data volume into a back-projected 3-D voxel space. Likewise, in the conventional implementation the measured data are stored by line-of-response in the array y_j , while in the Inverse Monte Carlo formulation the back-projected data is stored in an array which we also call y_j .

As in the conventional implementation, we can parse the expression for the ML/EM algorithm into 4 discrete steps per

iteration. The first step is forward projection, which in the conventional implementation consists of multiplying the system matrix by the most recent iteration of the reconstructed source distribution; as noted earlier, the Inverse Monte Carlo method substitutes the Monte Carlo generation of simulated events, followed by their event-by-event back-projection. This effectively *randomly samples from the system matrix*, with the system matrix re-interpreted to map from the reconstructed voxel space into back-projection space, rather than into lines-of-response. The next step is to take the ratio of observed to predicted projections: for the conventional implementation this is the ratio of events observed to predicted within each line-of-response, while in the re-interpretation it is the ratio of events observed to predicted *for each voxel within the back-projection space*. In each case, the dimension and index are the same in the numerator and denominator of the ratio expression.

The third step in each iteration of the ML/EM algorithm is usually termed "back-projection", which is not to be confused with the event-by-event back-projection which maps coincident detector coordinates into a 3-D back-projection space in our Inverse Monte Carlo formulation. Instead, this back-projection step maps the ratio matrix onto points in reconstruction space, by performing a weighted sum across

lines-of-response through a given voxel, weighted by the above ratio for each line-of-response and by the system matrix element. The effect of the back-projection step of the ML/EM algorithm is to sample from the ratio matrix according to the point spread function as expressed by the system matrix. In the conventional formulation, this entails forming a weighted average ratio, summing across the voxels within a given line-of-response; this weighted average gives the update ratio for that particular line-of-response.

Several Monte-Carlo based implementations of the back-projection step in the EM algorithm are possible, giving rise to several variants of the Inverse Monte Carlo reconstruction procedure. In the limit of an ideal spherical detector with perfect resolution, and in the limit of infinitesimal source and back-projection voxels, the system back-projection operator P_{ij} reduces to a very simple point spread function: $1/r^2$. The back-projection operation consists of convolving the source distribution with this point spread function. For a realistic detector geometry the point spread function is more complex, but it is implicitly contained within a Monte Carlo model of the detector geometry and the detector response. Therefore, one can perform the back-projection step of the ML/EM algorithm by *sampling from the ratio matrix according to the point spread function at each source voxel*. This may be accomplished by generating events according to the source voxel intensity distribution, and taking the weighted average of the ratio values within the back-projection voxels intersected by each generated event upon back-projection; the appropriate weighting factor is the chord length calculated during event-by-event back-projection. In the limit of many generated events, it will be seen that this forms the convolution of the ratio matrix with the point spread function at each source voxel, as desired. As in the forward-projection step, the number of generated events used to sample from the ratio matrix need be *no more than a few times the number of events in a given data sample*.

In practice, our Inverse Monte Carlo reconstruction method works quite well when using an approximation to the point spread function during the back-projection step. In fact, in the limit of a high-resolution detector (relative to the voxel size) the point spread function can be approximated by a delta function, so that the update ratio for a given source voxel is just given by the ratio matrix value at that point in back-projection space (assuming that the voxel size in back-projection space is the same as the voxel size in source space). This variant corresponds to an Inverse Monte Carlo implementation of the Image Space Reconstruction Algorithm as implemented by its authors; it is a local algorithm, in the sense that a discrepancy between back-projected data and the back-projection of a hypothesized source distribution at a given voxel affects the updating of *only that voxel*. More generally, one can approximate the effect of point-spread-function weighted sampling from the ratio matrix by simply forming a weighted sum of the ratio matrix values for a back-projection voxel and its nearest neighbors. It should be noted that the point spread function falls off rapidly for a high-resolution detector, so that the effect of ratio matrix values corresponding to distant voxels is slight.

II. METHODS OF IMPLEMENTATION

A. Back-Projection Methods

To test our reconstruction algorithm, we have generated test data from a software phantom, in conjunction with our Monte Carlo detector geometry and response model. Each test data "event" was then back-projected across a cubic lattice of 3D voxels; the result accumulated across many events was the test "back-projected data array" y_j . For applying the algorithm to real data collected with a real scanner, one would similarly back-project the data event-by-event into the array. In our Inverse Monte Carlo reconstruction, we iteratively compare the back-projection of simulated data (which is forward-projected from a hypothesized source distribution) with the back-projection of the "real" data as stored in the array y_j . Convergence is measured by the variance between the back-projected simulated data and the back-projected "real" data.

In the study detailed below, we back-projected each simulated event as it was detected into a 3D voxel array, using an algorithm discussed by Barresi et al [13]; the effect of this algorithm is to accumulate each voxel intercepted by a line segment between two detector hits according to the chord length by which each cubic voxel was intercepted. In conventional back projection-filtered (i.e. non-iterative) reconstruction of such high-resolution list mode data, the principal computational burden is that of performing this back-projection operation on each of the events. Thus we see that the total computational burden of our approach is a few times that required for event-by-event back-projection in non-iterative back projection-filtered reconstruction techniques. For lower-resolution systems, one could histogram (accumulate) a 3-D sinogram by the lines-of-response for Monte Carlo simulated events, then back-project from the histogram contents. In general, either pixel-driven or ray-driven back-projection algorithms could be used, as long as the same procedure is applied to Monte Carlo generated events and to measured data events.

We have chosen to set the first iteration of the hypothesized source distribution as the back-projected image of the data: $\lambda_i^{(1)} = y_i$. As noted earlier, we use the same voxel size in source distribution (object) space as in back-projection space. The same techniques should work in principle beginning from a uniform hypothesis $\lambda_i^{(1)} = \text{constant}$, but we see no point in ignoring the quite good approximation to the source distribution which is contained within the back-projection image. This choice also arose from our initial strategy of seeking to iteratively refine back-projection images obtained with detectors having a limited-angle geometry.

B. Sampling strategies

During each iteration of our reconstruction, we have generated a number of Monte Carlo events equal to the number of events within the entire hypothesized source distribution; voxels within the source distribution are visited sequentially rather than randomly, for convenience. A separate random number seed is stored for each source distribution voxel, so that the same events can be "removed" as were "generated" if the update ratio is found to be much less than unity for a given voxel. The average ratio of back-projected events to source hypothesis events increases with each iteration, with only a small number of voxels requiring

"removal" of previously-generated sample events. The number of back-projection space voxels and image space voxels were set equal for convenience, and our initial studies have been carried out with the fully local variant of the back-projection step which corresponds to the Image Space Reconstruction Algorithm.

IV. SIMULATIONS AND RESULTS

We have simulated 20 million events within an array of $64 \times 64 \times 32$ voxels each $1\text{mm} \times 1\text{mm} \times 1\text{mm}$, with Poisson fluctuations. We include 3 hot-spots with 8 times background intensity; these are cylinders of 6mm, 8mm, and 10mm diameter and lengths 1.5 times their diameter; this software phantom was chosen to match that used in previously-published work [8]. Detector resolution effects are not illustrated in the images shown, and are slight for the 2mm FWHM precision Positron-Emission Mammograph design (with depth-of-interaction sensitivity) for which this study was performed. The detector geometry consisted of 2 parallel plates each $11\text{cm} \times 11\text{cm}$, separated by 6cm. Reconstruction is insensitive to the detector geometry if a sufficient angular range of events are incorporated in the reconstruction. Results are shown in Figure 1.

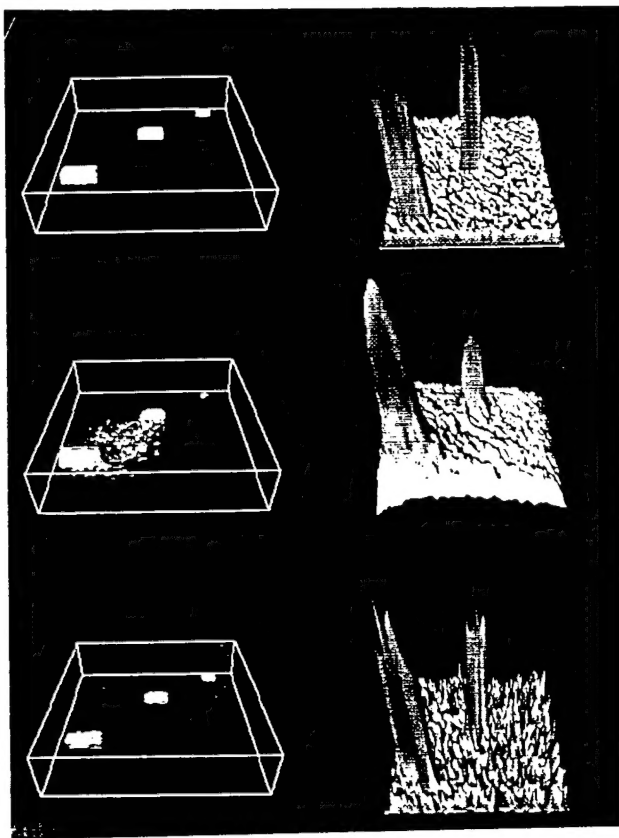


Figure 1: Reconstruction of a test software phantom. Top to bottom: Source distribution with Poisson fluctuations, back-projection image, Inverse Monte Carlo reconstructed image. Left to right: 3-D rendering above a threshold, horizontal slice across the phantom with the vertical axis indicating intensity.

In each figure, the left images are 3D renderings above a threshold from the same vantage point, while the right images show horizontal planar slices through the 3-D object (or reconstruction) with elevation indicating intensity. The topmost images shows the software phantom, with Poisson statistical fluctuations for 20 million events total. The next images down show 3-D back projection images of these events after detection with the dual-plane ideal detector; this back-projection accumulated the lengths of chords intersecting the voxels on a line connecting the two detection points. Finally, the bottommost images show our Inverse Monte Carlo reconstruction of events collected with the restricted-angle geometry ideal detector, after a total of 20 iterations. The total CPU time required was less than 15 minutes on a single-processor 100 MHz Alpha/AXP Workstation.

We have also performed tests on a more detailed and realistic software phantom, consisting of 69 ellipsoids of varying contrast to a uniform background, and with arbitrary orientation at fixed locations within a $128 \times 128 \times 64$ array of $2\text{mm} \times 2\text{mm} \times 2\text{mm}$ voxels [19]; this work is part of an ongoing effort to quantitatively validate and evaluate this reconstruction algorithm in the presence of realistic detector noise and other effects. Although this work is not yet complete, we were able use this complex phantom as a benchmark in testing the speed and convergence properties of this technique.

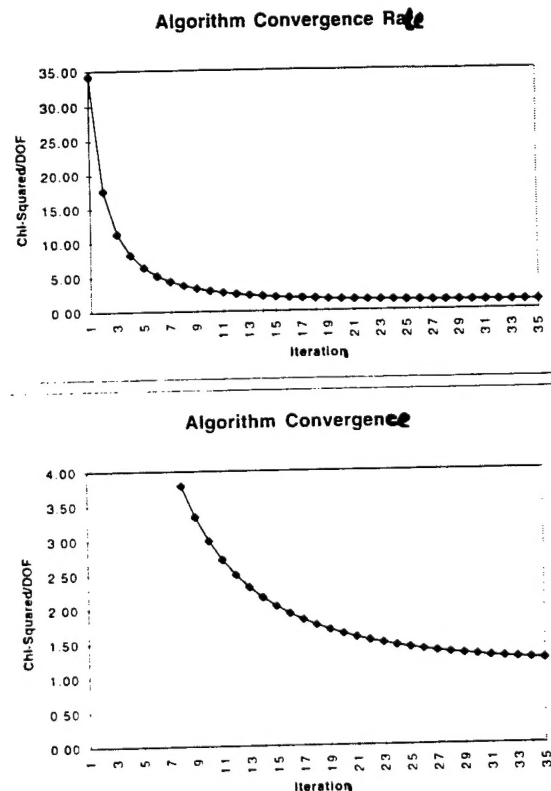


Figure 2: Convergence properties of Inverse Monte Carlo algorithm applied to complex software phantom. Top: Average Chi-squared per degree of freedom between "data" and "simulated" back projections as a function of iteration number. Bottom: Same with vertical axis expanded.

Figure 2 shows the convergence rate for our algorithm in reconstructing this complex software phantom, as measured by the average Chi-squared per degree of freedom between the "target" back-projection array (that of the back-projected "data" from the software phantom) and the "test" back-projection array (that produced by generating and back-projecting events according to the source hypothesis at each iteration). This measure scales properly with the statistical fluctuations which are present in the data distribution. It can be seen that after 15 iterations the differences between back-projected data and back-projected sample events gives an average Chi-squared per degree of freedom of less than 2. The time required to perform this calculation was less than 10 CPU minutes per iteration on our single-processor 100 MHz Alpha workstation, reconstructing 7 million events total within a 128 x 128 x 64 voxel array.

V. DISCUSSION AND CONCLUSIONS

As with any event-by-event back-projection technique, the CPU time required scales linearly with the number of events in the dataset. For our simple detector response model (which essentially included detector geometry only) the computational burden was dominated by the event-by-event back-projection of simulated events. This is a readily parallelizable step, and several groups have developed or are working on dedicated hardware to speed it significantly. The CPU time required for back-projection of events across the back-projection voxel array scales nearly linearly with the number of voxels intersected by a typical track, so that in moving from a 64 x 64 x 32 array to a 128 x 128 x 64 array one incurs only a factor of 2 increase in computational burden. We are currently working to extend this study to incorporate more realistic detector response effects and to apply it to real detector data.

VI. REFERENCES

- [1] Shepp LA and Vardi Y, "Maximum likelihood reconstruction in positron emission tomography," *IEEE Trans. on Med. Imag.*, vol. MI-1, pp.113-122, 1982.
- [2] Lange K and Carson R, "EM reconstruction algorithms for emission and transmission tomography," *J. Comput. Assist. Tomogr.*, vol. 8, pp.306-316, 1984.
- [3] Lewitt R and Muehllehner G, "Accelerated iterative reconstruction for positron emission tomography based on the em algorithm for maximum likelihood estimation," *IEEE Trans. on Med. Imag.*, vol. MI-5, pp.16-22, 1986.
- [4] Johnson C, Yan Y, Carson R, Martino R, and Daube-Witherspoon M, "A system for the 3D reconstruction of retracted-septa PET data using the EM algorithm," *IEEE Trans. on Med. Imag.*, vol. 42, pp.1223-1227, 1995.
- [5] Chen C and Lee S-, "Optimal data replication: A new approach to optimizing parallel EM algorithms on a mesh-connected multiprocessor for 3D PET image reconstruction," *IEEE Trans. on Med. Imag.*, vol. 42, pp.1235-1245, 1995.
- [6] Guerrero T, Levin C, Huang S, Dahlbom M, Cherry S, and Hoffman E, "Implementation and evaluation of the EM algorithm for 3D PET," *J. Nucl. Med.*, vol. 35, p.1871, 1994. (Abstract)
- [7] Hudson HM and Larkin RS, "Accelerated image reconstruction using ordered subsets of projection data," *IEEE Trans. on Med. Imag.*, vol. MI-13, pp. 601-609, 1994.
- [8] Thompson CJ, Murthy K, Picard Y, Weinberg IN, and Mako F, "Positron Emission Mammography (PEM): A promising technique for detecting breast cancer," *IEEE Trans. on Nucl. Sci.*, vol. 42, pp.1012-1016, 1995.
- [9] Townsend DW, Schorr B, and Jeavons A, "Three-dimensional image reconstruction for a positron camera with limited angular acceptance," *IEEE Trans. on Nucl. Sci.*, vol. 27, pp.463-470, 1980.
- [10] Suzuki S and Yamaguchi S, "Comparison between an image reconstruction method of filtering backprojection and the filtered backprojection method," *Applied Optics*, vol. 27, pp.2867-2870, 1988.
- [11] Hogan, Harvey PJ, Howse DC, McKee BTA, "Image reconstruction for a 3D PET system using a minimum norm constraint," *Phys. Med. Biol.*, vol. 36, pp.35-46, 1991.
- [12] Zeng L and Gullberg GT, "Can the backprojection filtering algorithm be as accurate as the filtered backprojection algorithm?," *Conf. Rec. of IEEE Med. Imag. Conf.*, vol. 3, pp.1232-1236, Norfolk, 1994.
- [13] Barresi S, Bollini D, and Del Guerra A, "Use of a transputer system for fast 3-D image reconstruction in 3-D PET," *IEEE Trans. on Nucl. Sci.*, vol. 37, pp.812-816, 1990.
- [14] Di Lecce V, Di Sciascio E, and Manni AR, "A pipeline backprojector for on-line 3-D PET," *Conf. Rec. of IEEE Med. Imag. Conf.*, vol. 2, pp.1069-1073, San Francisco, 1995; and Di Lecce V, Di Sciascio E, and Manni AR, "Parallelization of 3-D PET Bp/F Reconstruction on a DSP Cluster," *Conf. Rec. of IEEE Med. Imag. Conf.*, vol. 2, pp.1222-1226, San Francisco, 1995.
- [15] Daube-Witherspoon ME and Muehllehner G, "An iterative image space reconstruction algorithm suitable for volume ECT," *IEEE Trans. on Med. Imag.*, vol. MI-5, pp. 61-66, 1986.
- [16] Floyd CE and Jaszczak RJ, "Inverse Monte Carlo: A unified reconstruction algorithm for SPECT," *IEEE Trans. on Nucl. Sci.*, vol. 32, pp.779-785, 1985.
- [17] Levin CS, Dahlbom M, and Hoffman EJ, "A Monte Carlo correction for Compton scattering effects in 3D PET brain imaging," *Conf. Rec. of IEEE Med. Imag. Conf.*, vol. 4, pp.1502-1506, Norfolk, 1994.
- [18] Levin CS, Tai Y-C, Hoffman EJ, Dahlbom M, and Farquhar TH, "Removal of the effect Compton scattering in 3-D whole body positron emission tomography by Monte Carlo," *Conf. Rec. of IEEE Med. Imag. Conf.*, vol. 2, pp.1050-1054, San Francisco, 1995.
- [19] Furuie SS, Herman GT, Narayan TK, Kinahan PE, Karp JS, Lewitt RM and Matej S, "A methodology for testing for significantly significant differences between fully 3D PET reconstruction algorithms," *Phys. Med. Biol.*, vol. 39, pp.341-354, 1994.